**NTNU – Trondheim**
Norwegian University of
Science and Technology

# Terahertz Time-Domain Spectroscopy

Hans Christian Bakken Skjeie

Master of Science in Electronics
Submission date: July 2012
Supervisor: Ulf Lennart Østerberg, IET

Norwegian University of Science and Technology
Department of Electronics and Telecommunications

# Abstract

The field of terahertz time-domain spectroscopy (THz-TDS) is still far from reaching its full potential, but is a very promising utility for a wide range of applications. Principle experiments have been performed in fields of drug screening, pharmaceutical, medical diagnostics, security imaging and detection of explosives. Optimized and adapted THz-TDS systems holds great promise for driving this technology further.

The purpose of this thesis was to build a THz-TDS system, explore possibilities for improving this system and to perform THz-TDS measurements on semiconductors and wood. The aim of the experimental work was to build a stable and reliable system with an electric field strength of THz radiation in the order of $\frac{\mathrm{kV}}{\mathrm{cm}}$. The THz-TDS system used in this thesis was based upon the principles of optical rectification and free-space electro-optic sampling in zinc telluride (ZnTe) crystals using a femtosecond Ti:Sapphire amplified laser.

Theoretical studies were performed on the principles of generation and detection of THz radiation. The experimental work was based on publications of similar experiments. Theoretical and experimental studies lead to several modifications and improvements of the setup first built in this thesis. Experiments were performed on disparate materials to find suitable materials for THz transmission. Results from measurements performed on semiconductors and wood, obtained by THz-TDS, were analysed to find the absorption coefficient and the refractive index of the materials. The spectroscopic information obtained by THz-TDS can also be used to find the conductivity and the mobility of these materials.

THz-TDS measures the electric field and therefore provides information of both the amplitude and the phase of the THz wave. A Fourier transformation was used to obtain the frequency spectrum of the detected signal. The improvements were done by analysing the results of the detected signal to see which adjustments and modifications to the setup that had positive effects on the results. The pump power used for generation of THz radiation and the optimum azimuthal angle of the ZnTe crystals were crucial to obtain a THz-TDS system with a strong electric field. The maximum electric field strength for the THz radiation in this thesis was $13.2\frac{\mathrm{kV}}{\mathrm{cm}}$, with a signal-to-noise ratio of 43 and dynamic range of 1500.

# Sammendrag

Terahertz tidsdomenet spektroskopi (THz-TDS) er fortsatt langt fra å nå sitt fulle potensialet, men er et meget lovende verktøy for et bredt spekter av bruksområder. Eksperimenter har blitt utført innenfor områder som narkotika søking, farmasi, medisinsk diagnostikk, sikkerhets avbildning og deteksjon av eksplosiver. Optimaliserte og tilpassede THz-TDS systemer har veldig lovende utsikter for å drive denne teknologien videre.

Hensikten med denne oppgaven var å bygge et THz-TDS system, utforske muligheter for å forbedre dette oppsettet og utføre tidsdomenet spektroskopi målinger på halvledere og treverk. Målet med det eksperimentelle arbeidet var å bygge et stabilt og pålitelig oppsett med et sterkt elektrisk felt av THz stråling i størrelsesordenen $\frac{\text{kV}}{\text{cm}}$. THz-TDS oppsettet brukt i denne oppgaven var basert på prinsippene om optisk rektifikasjon og elektrooptisk deteksjon i zinc telluride (ZnTe) krystaller ved bruk av en femtosekund Ti:Sapphire laser.

Teoretiske studier ble gjort rundt prinsippene av generering og detektering av THz. Det eksperimentelle arbeidet ble basert på publikasjoner av lignende arbeid. Teoretiske og eksperimentelle studier førte til flere modifikasjoner og forbedringer av oppsettet som først ble bygd i denne oppgaven. Eksperimenter ble gjort på ulike typer materialer for å finne passende materialer for transmisjon av THz stråling. Resultater fra målinger gjort på halvledere og treverk, innhentet fra THz-TDS, ble analysert for å finne absorpsjons koeffisienten og brytningsindeksen til materialene. Den spektroskopiske informasjonen som kan bli innhentet fra THz-TDS kan også bli brukt til å finne konduktiviteten og mobiliteten til disse materialene.

THz-TDS måler det elektriske feltet og kan derfor gi informasjon om både amplituden og fasen til THz strålingen. En Fouriertransformasjon ble benyttet på det detekterte signalet for å finne frekvensspekteret. Forbedringer ble gjort ved å analysere resultatene for å se hvilke justeringer og modifikasjoner av oppsettet som forbedret målingene. Effekten av den optiske pumpen brukt for å generere THz stråling og de optimalene vinklene for ZnTe krystallene var avgjørende for å oppnå et THz-TDS system med et sterkt elektrisk felt. Den maksimale elektriske feltstyrken av THz stråling som ble oppnådd i denne oppgaven var $13.2\frac{\text{kV}}{\text{cm}}$, med et signal-støy-forhold på 43 og en dynamisk rekkevidde på 1500.

# Acknowledgements

I would like to acknowledge a lot of nice people I was lucky to work with during my master's studies.

First, I would like to express special thanks to my advisor, Professor Ulf Österberg at NTNU. His endless patience, guidance and curiosity made the laboratory a place where I could really flourish. From Ulf I've learned a zillion things about lasers and optics in general, and THz technology in particular. Ulf is not only an excellent professor and researcher, but a truly great advisor and cares for his students. It's been a real privilege to work for and with Ulf.

I would also like to express special thanks to my great lab partner Lisa Henriksen, who also has become a good friend. She kept the lab fun with her humour and great spirit in those long days you need a little extra to keep you going. Lisa is a person with a lot of good ideas and is always helpful.

My dear classmates, Nils Jacob Sand and Pål Andersen, should also be acknowledged for being great friends through all the years at NTNU and made the long hours at the office more durable. It has also been great to know José Muñoz, who's dedication to work in the laboratory was admirable and he has a great sense of humour.

I would also like to say thanks to the guys in the workshop at the electronics department at NTNU, Tore Landsem and Tore Berg, for helping out with equipment and components.

Lastly and most important, I would like to thank my family and friends. Mom and dad, thank you for all your moral and financial support. To all my great friends, thank you for ensuring I had something that resembled a social life outside of school.

# Contents

# List of Figures

# List of Tables

# Chapter 1

# Introduction

The study of ultrafast carrier dynamics and relaxation processes in semiconductors and nanostructures are very important to improve today's technology and for producing the next generation electronic and optic devices for computing and communications systems. Information and communications technology benefits from THz technology where it is used for a wide range of applications, such as wireless communication, high-speed data processing, satellite communication and better spatial resolution for imaging. During the mid-70's, time-dependent spectroscopy of semiconductors was established by Schank and Ippen at Bell laboratories using picoseconds laser pulses. Ever since the pioneering work of D.H. Auston and co-workers in the 1980s, terahertz time-domain spectroscopy (THz-TDS) has had an increasing interest in science and research. The development of THz sources was mainly driven by two scientific groups; Time-domain spectroscopists who searched for longer wavelengths, and radio-astronomers who wanted shorter wavelengths to work with [16]. Astronomers are interested in terahertz technology to study photons and particles in the atmosphere. The electromagnetic spectrum of terahertz waves lies between the microwave and infrared regions, but has not been easily accessible due to lack of efficient sources and detectors.

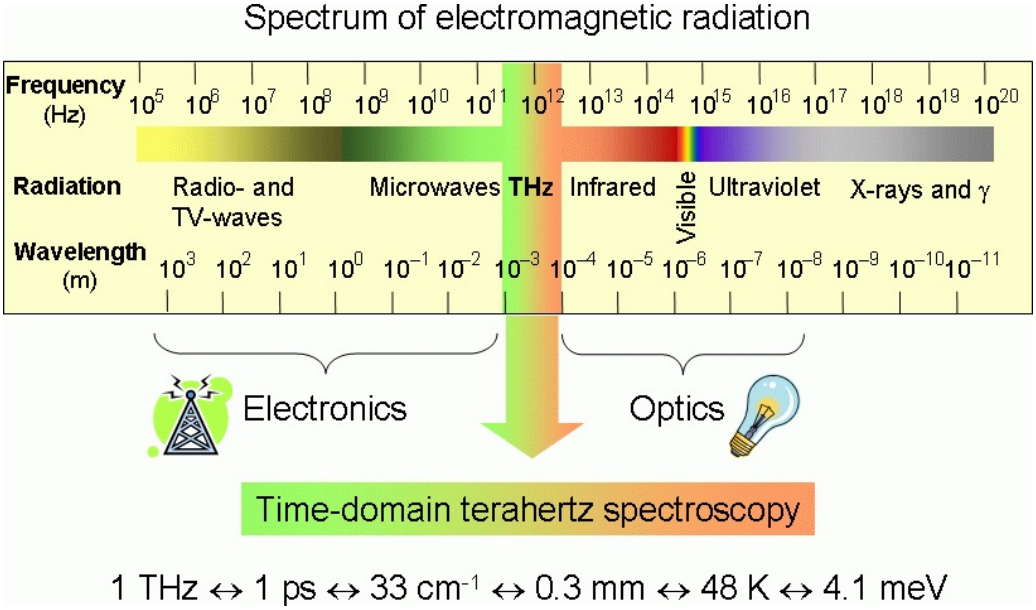


Figure 1.1: Spectrum of electromagnetic radiation [25].

As seen in figure 1.1, a frequency of $10^{12}$ Hz , or 1 THz, corresponds to a wavelength of 300 $\mu$m (33 $cm^{-1}$) and a period of 1 picosecond. It has a photon energy of 4.1 meV and corresponds, through the Boltzmann constant, to a thermal energy at a temperature of 48 Kelvin [16]. THz radiation is loosely defined as the frequency between 0.1-10 THz and was known as the "THz gap" since one could not access this region efficiently for a long time. The THz technology has advanced in conjunction with the tremendous progress in the laser equipment during the recent years, and today it is possible to get stable and relatively small laser systems capable of producing and detecting THz radiation [13].

THz-TDS is based on the generation of subpicosecond THz pulses using ultrashort near-infrared laser pulses with durations in the order of 10's of femtoseconds. THz radiation excites the low-frequency vibrations in molecules and is therefore sensitive to small bonding forces and high masses. The spectroscopic information that can be obtained by THz-TDS combined with imaging techniques has a high potential in many areas of applications, such as pharmaceutical, drug screening, medical diagnostics and detection of explosives. One of the most prominent advantages of THz imaging is its ability to penetrate a wide range of materials, such as paper, wood, plastics, fabric, ceramics, semiconductors and many others that are opaque in the visible and near-infrared region (NIR). Terahertz radiation can penetrate up to several millimetres of tissue with low water content and its sensitivity to water absorption makes it a promising probe for certain types of cancer. The energy of terahertz radiation is too low to cause any damage to tissue; it is non-ionizing, unlike X-rays. This makes terahertz radiation suitable for medical imaging and security imaging. Principle experiments have been performed in all of these fields. With optimized and adapted THz systems, there are a great potential for these applications.

Even though the THz technology is far from reaching its full potential, the advancements in the recent years are very promising. In the field of medical imaging, most of the technology is already available and has been tested for scanning certain tumour cells. Experiments have been performed to find the extent and depth on surface and sub-surface on some tumour cells with positive results. In May 2012, a new record was set in the field of telecommunications with a wireless data transfer rate of 3 Gigabits per second at 542 GHz using THz technology. Proof-of-concept has been achieved for the fields of security imaging, weapons imaging and detection of explosives. In the following years, it is expected that THz technology will have a significant impact in all of these fields.

The goal for this master's thesis was to build a setup for THz time-domain spectroscopy, optimize this setup and perform measurements on semiconductors and wood. THz radiation was generated through optical rectification in a ZnTe crystal and detected through electro-optic detection using another ZnTe crystal. A study was performed on how the conversion efficiency of the generation crystal and how the detection crystal depended on the azimuthal angle. Various methods were used to optimize the setup for the THz-TDS before the final results could be acquired. THz-TDS measures the electric field strength of THz radiation indirectly through free-space electro-optic sampling, which provides information of both the amplitude and the phase. Measurements obtained by THz-TDS are done in the time-domain and then converted to the frequency-domain using a Fourier transformation (FT). THz-TDS requires reference data acquired in the same way as the sample data to compare the results. The absorption coefficient and the refractive index were calculated from the obtained frequency spectrum. The spectroscopic information obtained by THz-TDS also provides data to calculate the conductivity and mobility of the materials [23].

# About this work

This thesis is organized as follows:

Chapter 1 is an introduction to this thesis.

Chapter 2 will review the basic principles and physics involved in the generation and detection of THz radiation.

Chapter 3 describes the theoretical background and setup of a THz time-domain spectroscopy system. Detailed information of the necessary instruments, generation and detection of THz radiation and data analysis will be elaborated in this chapter.

Chapter 4 will present the results and discussion of the experimental studies.

Chapter 5 gives an outlook to further ideas and future work.

Chapter 6 is a conclusion of the theoretical and experimental studies of this thesis.

# Chapter 2

# Principles of generation and detection of electromagnetic transients in non-linear crystals

## 2.1 Maxwell's equations. Wave equation and its solution in the far field

Electromagnetic phenomena obey and are governed by Maxwell's equations. In the following equations from reference [31], bold characters represent vectors and normal characters represent scalars. The equations for vacuum can be written in the form

$$\nabla \cdot \mathbf{E} = \frac{\rho}{\epsilon_0}, \tag{2.1}$$

$$\nabla \times \mathbf{E} = -\frac{\partial \mathbf{B}}{\partial t}, \tag{2.2}$$

$$\nabla \cdot \mathbf{B} = 0, \tag{2.3}$$

$$\nabla \times \mathbf{B} = \mu_0 \epsilon_0 \frac{\partial \mathbf{E}}{\partial t} + \mu_0 \mathbf{J}, \tag{2.4}$$

where $\mathbf{E}$ is the strength of the electric field, $\mathbf{B}$ is the magnetic induction, $\mathbf{J}$ is the current density, $\rho$ the charge density, $\mu_0$ is the magnetic permeability of vacuum, $\epsilon_0$ is the electric permittivity of vacuum and t is the time. The speed of light in vacuum, c, can be related through the relation $c = \sqrt{\mu_0 \epsilon_0}^{-1}$. The charge conservation law can be obtained by using the identity $\nabla \cdot (\nabla \times \mathbf{B}) = 0$ on the eq. 2.4 and the time derivative of the eq. 2.1.

$$\frac{\partial \rho}{\partial t} = \nabla \cdot \mathbf{J}. \tag{2.5}$$

The charge density $\rho$ in a medium can be written as a sum of the external charges (free electrons) $\rho_{ext}$ and the polarized charges $\rho_{pol}$, and related to the polarization density $\mathbf{P}$.

$$\rho = \rho_{ext} + \rho_{pol}, \tag{2.6}$$

$$\rho_{pol} = -\nabla \cdot \mathbf{P}. \tag{2.7}$$

The sum of the conduction $\mathbf{J}_{cond}$ and displacement $\mathbf{J}_{disp}$ current densities gives the total current $\mathbf{J}$. $\mathbf{J}_{disp}$ can be related to the polarization density $\mathbf{P}$ as

$$\mathbf{J} = \mathbf{J}_{cond} + \mathbf{J}_{disp}, \tag{2.8}$$

$$\mathbf{J}_{disp} = \frac{\partial \mathbf{P}}{\partial t}. \tag{2.9}$$

The electric displacement $\mathbf{D}$ and magnetic field strength $\mathbf{H}$ are the material-related parameters, which for a linear isotropic non-magnetic dielectric are given by

$$\mathbf{D} = \epsilon \mathbf{E} = \epsilon_0 \mathbf{E} + \mathbf{P} = \epsilon_0 (1 + \chi)\mathbf{E}, \tag{2.10}$$

$$\mathbf{H} = \frac{\mathbf{B}}{\mu_0}, \tag{2.11}$$

where $\epsilon$ is the dielectric constant and $\chi$ the dielectric susceptibility. The polarization density can then be expressed by the relationship

$$\mathbf{P} = (\epsilon - 1)\epsilon_0 \mathbf{E} = \epsilon_0 \chi \mathbf{E}. \tag{2.12}$$

Maxwell's equations can be rewritten by taking into account the material parameters and equations 2.5 - 2.11.

$$\nabla \cdot \mathbf{D} = \frac{\rho_{ext}}{\epsilon_0}, \tag{2.13}$$

$$\nabla \times \mathbf{E} = -\frac{\partial \mathbf{B}}{\partial t}, \tag{2.14}$$

$$\nabla \cdot \mathbf{B} = 0, \tag{2.15}$$

$$\nabla \times \mathbf{H} = \mathbf{J}_{cond} + \epsilon_0 \frac{\partial \mathbf{D}}{\partial t}. \tag{2.16}$$

Equations 2.13 - 2.16 are called material Maxwell's equations. The conduction current $\mathbf{J}_{cond}$ and the polarization $\mathbf{P}$ are included into the displacement $\mathbf{D}$. These parameters are the only time-varying parameters, and are describing the response of the medium to the electromagnetic field. In the absence of free charges, Maxwell's material equations can be combined into

$$\nabla^2 \mathbf{E} - \frac{1}{c^2} \frac{\partial^2 \mathbf{E}}{\partial t^2} = \mu_0 \left(\frac{\partial \mathbf{J}_{cond}}{\partial t} + \frac{\partial^2 \mathbf{P}}{\partial t^2}\right). \tag{2.17}$$

This equation is called the wave equation, since it describes the propagation of an electromagnetic wave. The two time-varying source terms are the conduction current $\mathbf{J}_{cond}$ and the polarization $\mathbf{P}$. The far-field on-axis solution of equation 2.17 relates the temporal shape of an electromagnetic signal emitted by a slab of material with a time-varying spatially uniform conduction current $\mathbf{J}_{cond}$ and/or the polarization $\mathbf{P}$ at the axis normal to the slab at a distance. This solution has been presented by several authors and can be found in reference [31] and [29].

$$\mathbf{E}_{rad}(t) \approx -\frac{\mu_0}{4\pi}\frac{S}{z}\left(\frac{\partial \mathbf{J}_{cond}(t)}{\partial t} + \frac{\partial^2 \mathbf{P}(t)}{\partial t^2}\right). \tag{2.18}$$

S is the emitting area and z stands for the distance between the emitter surface and the detection point. This solution is important since it allows for reconstruction of the polarization and carrier dynamics in an electromagnetic signal, under the assumption that the radiated field is properly detected.

## 2.2 Linear and non-linear contributions to polarization

Considering eq. 2.12 in the linear case, the polarization P can be expressed as [31]

$$P(r,t) = \int_{-\infty}^{\infty} \chi^{(1)}(r-r', t-t')E(r',t')\,\mathrm{d}r'\,\mathrm{d}t', \tag{2.19}$$

where $\chi^{(1)}$ is the linear susceptibility and a $2^{nd}$ rank tensor. If we assume that the electric field has the form of a monochromatic plane wave

$$E(r,t) = E(k,\omega) = E_0(k\omega)\cdot e^{(ik\cdot r - i\omega t)}, \tag{2.20}$$

where $E_0$ is the electric field amplitude, k is a wavenumber, $\omega$ is the angular frequency and r is a coordinate. Then the Fourier transformation of eq. 2.20 gives us

$$P(r,t) = P(k,\omega) = \chi^{(1)}(k,\omega)E(k,\omega). \tag{2.21}$$

The dielectric constant is then

$$\epsilon(k,\omega) = 1 + \frac{\chi^{(1)}}{\epsilon_0}(k,\omega). \tag{2.22}$$

In the non-linear case the eq. 2.21 can be expanded into a powers series of E:

$$\begin{aligned} P(r,t) = &\int_{-\infty}^{\infty} \chi^{(1)}(r-r', t-t')E(r',t')\,\mathrm{d}r'\,\mathrm{d}t' \\ &+ \int_{-\infty}^{\infty} \chi^{(2)}(r-r_1, t-t_1; r-r_2, t-t_2) \\ &\times E(r_1,t_1)E(r_2,t_2)\,\mathrm{d}r_1\,\mathrm{d}t_1\,\mathrm{d}r_2\,\mathrm{d}t_2 + \ldots, \end{aligned} \tag{2.23}$$

where $\chi^{(i)}$ stands for the i-*th* order non-linear susceptibility, representing the tensor of the (i+1) - *th* rank. By taking the Fourier transformation of eq. 2.23, the k and $\omega$ dependent polarization can be written as

$$P(k,\omega) = P^{(1)}(k,\omega) + P^{(2)}(k,\omega) + P^{(3)}(k,\omega) + \dots \tag{2.24}$$

with

$$\begin{aligned} P^{(1)}(k,\omega) &= \chi^{(1)}(k,\omega)E(k,\omega), \\ P^{(2)}(k,\omega) &= \chi^{(2)}(k=k_i+k_j, \omega=\omega_i+\omega_j)E(k_i,\omega_i)E(k_j,\omega_j), \\ P^{(3)}(k,\omega) &= \chi^{(3)}(k=k_i+k_j+k_k, \omega=\omega_i+\omega_j+\omega_k) \times E(k_i,\omega_i)E(k_j,\omega_j)E(k_k,\omega_k). \end{aligned} \tag{2.25}$$

The equations above clearly shows that non-linear susceptibilities of the order higher than 1 provide mixing of the frequencies of the different monochromatic waves, if their wave vectors match (phase matching). Keeping the phase matching in mind, these equations can be rewritten into the conventional tensor form:

$$\begin{aligned} P_i^{(1)}(\omega) &= \chi_{ij}^{(1)}(\omega)E_j(\omega), \\ P_i^{(2)}(\omega=\omega_j\ \omega_k) &= \chi_{ijk}^{(2)}(\omega)E_j(\omega)E_k(\omega), \\ P_i^{(3)}(\omega=\omega_j+\omega_k+\omega_l) &= \chi_{ijkl}^{(3)}(\omega)E_j(\omega)E_k(\omega)E_l(\omega). \end{aligned} \tag{2.26}$$

An estimation for the ratio of two successive polarization terms of the series in eq. 2.23 can be expressed as

$$\left|\frac{P^{(n+1)}}{P^{(n)}}\right| = \left|\frac{\chi^{(n+1)}E}{\chi^{(n)}}\right| \approx \left|\frac{E}{E_{mat}}\right|, \tag{2.27}$$

where $E_{mat}$ is the inherent electric field inside the medium and is typically in the order of $10^8 \frac{V}{cm}$. Therefore $\frac{\chi^{(n+1)}}{\chi^{(n)}} \approx E_{mat}^{-1}$ and the higher-order contributions to the non-linear polarization will always be much weaker than the lower-order ones. The internal symmetry of the medium determines the form of the $\chi^{(n)}$ tensor. In materials with inversion symmetry $\chi^{(2n)} = 0$, where $n = 1, 2, 3, \dots$, the non-linear polarization therefore contains only odd-order terms. A medium with inversion symmetry contains a regular lattice of points such that inversion leaves the crystal structure unchanged (invariant). By inversion it means replacing each atom at a coordinate $\overrightarrow{r}$, relative to the point, with the one with $-\overrightarrow{r}$. If the even-number higher-order polarization $P_{\overrightarrow{r}}^{(2n)} = \chi^{(2n)}E^{(2n)}$ is induced to this medium along the direction $\overrightarrow{r}$, inversion symmetry implies that the polarization $P_{-\overrightarrow{r}}^{(2n)} = \chi^{(2n)}E^{(2n)}$ along the direction $-\overrightarrow{r}$ should be equal to $P_{\overrightarrow{r}}^{(2n)}$ in its absolute value. It should also have an opposite sign. Given the even power of the electric field, this can only be possible if $\chi^{(2n)} = 0$. The even order processes are symmetry allowed in the non-centrosymetric materials [31] [29].

## 2.3 Optical rectification and second harmonic generation

Optical rectification is a non-linear process which occurs when an intense optical beam passes through a medium and generation of DC polarization occurs. Optical rectification is a second-order phenomenon, known as difference frequency generation (DFG). Instead of having two monochromatic beams in DFG, in many cases it is enough to have a high-power beam with a properly broad spectral bandwidth. If the applied electric field is delivered by a femtosecond laser, the spectral bandwidth is very large and is therefore appropriate for generation of THz waves. It is based on optical pumping of optically transparent non-linear materials and the difference frequency interaction takes place under optical rectification of the femtosecond pulses here [18]. A polarization is produced by the mixing of different frequency components and results in emission of electromagnetic waves in the terahertz region. This generation of THz radiation can be understood as a phase-matched non-linear optical $\chi^{(2)}$ process [20].

Optical rectification is a difference frequency generation and only non-centrosymmetric non-linear materials can be used to generate THz emission, since the non-linear susceptibility $\chi^2 = 0$ for centrosymmetric crystals. When the ultrashort pulses propagates through a non-linear crystal, the input field cause the atoms to develop an oscillating dipole moment and radiate. This section will focus on the non-linear $2^{nd}$ order polarization induced by an optical excitation. If we now assume that we have two plane electromagnetic waves $E_1(t) = A_1(t)cos(\omega_1 t)$ and $E_2(t) = A_2(t)cos(\omega_2 t)$ incident on a material, where $A_{1,2}(t)$ are the wave envelopes and $\omega_{1,2}$ are the carrier frequencies. The $2^{nd}$ order non-linear polarization $P^{(2)}$ from eq. 2.26 can then be written as

$$\begin{aligned} P^{(2)}(\omega = \omega_1 + \omega_2) = & \\ &= \chi^{(2)}_{ijk}(\omega)A_1(t)A_2(t)cos(\omega_1 t)cos(\omega_2 t) \\ &= \frac{1}{2}\chi^{(2)}_{ijk}(\omega)A_1(t)A_2(t)(cos[(\omega_1 - \omega_2)t] + cos[(\omega_1 + \omega_2)t]) \\ &= P^{(2)}_{\Delta}(\omega) + P^{(2)}_{\sum}(\omega). \end{aligned} \tag{2.28}$$

$P^{(2)}(\omega)$ now consists of the two terms $P^{(2)}_{\Delta}(\omega)$ and $P^{(2)}_{\sum}(\omega)$, which contains the *difference* and *sum* frequencies. When the two electromagnetic waves are identical, i.e. $A_1 = A_2 = A$ and $\omega_1 = \omega_2 = \omega$. The equation 2.28 will be reduced to

$$\begin{aligned} P^{(2)}(2\omega = \omega + \omega) = &\quad \frac{1}{2}\chi^{(2)}_{ijk}(2\omega)A^2(t) + \frac{1}{2}\chi^{(2)}_{ijk}(2\omega)A^2(t)cos(2\omega t) = \\ &= P^{(2)}_{\Delta}(0) + P^{(2)}_{\sum}(2\omega). \end{aligned} \tag{2.29}$$

The result of equation 2.29 consists of two non-zero polarization terms, where both are dependent on the electric field amplitude. The term $P^{(2)}_{\Delta}(0)$ describes the effect called *optical rectification*, and is completely independent of the carrier frequency. The term $P^{(2)}_{\sum}(2\omega)$ describes the effect called *second harmonic generation* (SHG), which contains oscillations at the doubled carrier frequency. $P^{(2)}_{\Delta}$, which is the carrier-frequency-independent second-order polarization term, is proportional to the square of the electromagnetic wave amplitude, i.e. directly

proportional to the wave intensity [31]. The electromagnetic wave is unmodulated when, i.e. $A(t) = const$, and the optical rectification effect will result in a permanent polarization inside the medium. The term $P_{\Delta}^{(2)}$ will be time-dependent in the case of a pulsed electromagnetic wave. According to the wave equation (2.17) this will result in electromagnetic radiation with the far-field time-varying electric field strength given by eq. 2.18. This property will be used in this thesis to generate THz electromagnetic signals in non-linear crystals. Not all non-linear optical crystals have both good optical rectification efficiencies and SHG. Good phase matching over a very wide frequency range over a considerable optical path inside the crystal is required for the co-propagation of the carrier, second harmonic and optically rectified signals, which is not the case for most dielectrics. The non-linear optical crystals with a high optical rectification efficiency often have very small SHG efficiency and vice versa.

The wave equation that describes the propagation of the electric field is given by

$$\bigtriangledown^2 E - \mu_0 \frac{\partial^2 D^{(1)}}{\partial t^2} = \mu_0 \frac{\partial^2 P_{NL}}{\partial t^2}, \tag{2.30}$$

where $D^{(1)} = \epsilon E$ is the first-order displacement field [9].

## 2.4 Electro-optic detection

Electro-optic detection is a second-order non-linear process where an applied electric field induces a change in the refractive index in an electro-optic material at visible near-IR frequencies that is proportional to the applied field [26]. It is based on the linear electro-optic effect, known as the Pockels effect. Free-space electro-optic sampling is capable of providing very high speed detection and it resolves the coherent, time-dependent electric field, so phase information is retained. This gives us the ability to extract both the refractive index and absorption coefficient from the detected signal. To get the temporal profile, the signal is recorded by repeating the measurement as the delay of the laser pulse is varied. A typical setup for electro-optic detection is shown in figure 3.11.

The following calculations can be found in the references [40] and [31]. The optical dielectric constant of a medium $\epsilon(\omega, E_0)$ will be a function of the amplitude of the applied field $E_0$ in the case where a low-frequency, $\Omega$, or a DC electric field $E_0(\omega \approx 0)$ is applied to the medium. If the applied field $E_0$ has a small amplitude, $\epsilon(\omega, E_0)$ can be expressed as a power series of $E_0$ [28]:

$$\epsilon(\omega, E_0) = \epsilon^{(1)} + \epsilon^{(2)}(\omega + \Omega)E_0 + \epsilon^{(3)}(\omega + 2\Omega)E_0 E_0 + \ldots \tag{2.31}$$

Since $D = \epsilon E + \frac{P}{\epsilon_0}$ and $P = \chi^{(1)}E + \chi^{(2)}E^2 + \ldots$, the non-linear terms of the optical dielectric constant are

$$\begin{aligned} \epsilon^{(2)}(\omega + \Omega) &= \tfrac{1}{\epsilon_0}\chi^{(2)}(\omega + \Omega), \\ \epsilon^{(3)}(\omega + 2\Omega) &= \tfrac{1}{\epsilon_0}\chi^{(3)}(\omega + 2\Omega), \\ &\ldots \end{aligned} \tag{2.32}$$

The electro-optic effect for a medium with no inversion symmetry will be dominated by the linear term $\epsilon^{(2)}E_0$. This effect is called the *linear electro-optic effect*, or the *Pockels effect*. In any type of medium there will also exist another effect, called the *Kerr effect*, which is the quadratic electric field term $\epsilon^{(3)}E_0E_0$. If we now consider the linear electro-optic effect in a crystalline medium. Without an applied electric field, the spatial dispersion of a refractive index $n = \sqrt{\epsilon}$ of the crystal is described by a refractive index ellipsoid.

$$\frac{x^2}{n_x^2} + \frac{y^2}{n_y^2} + \frac{z^2}{n_z^2} = 1, \tag{2.33}$$

where x,y and z are the principal dielectric axes, i.e the axes along which D and P are collinear. The dielectric tensor changes in the presence of an external electric field $E_0(x, y, z)$, which results in a difference in the refractive index. An induced birefringence in the crystal, caused by the external field, will alter the refractive index of the propagating electromagnetic waves polarized along and perpendicularly to the applied field. The refractive index ellipsoid will be affected by the applied electric field and can be expressed by the changes in the constants $\frac{1}{n_x^2}$, $\frac{1}{n_y^2}$ and $\frac{1}{n_z^2}$. By using the conventions of [31] and [40], the new (deformed) index ellipsoid can be expressed as

$$\Big(\frac{1}{n^2}\Big)_1 x^2 + \Big(\frac{1}{n^2}\Big)_2 y^2 + \Big(\frac{1}{n^2}\Big)_3 z^2 + 2\Big(\frac{1}{n^2}\Big)_4 yz + 2\Big(\frac{1}{n^2}\Big)_5 xz + 2\Big(\frac{1}{n^2}\Big)_6 xy = 1. \tag{2.34}$$

Without an applied electric field and by choosing the axes x, y, z parallel to the crystal principal dielectric axes, equation 2.34 will be reduced to equation 2.33 and

$$\Big(\frac{1}{n^2}\Big)_1\Big|_{E_0=0} = \frac{1}{n_x^2}; \Big(\frac{1}{n^2}\Big)_2\Big|_{E_0=0} = \frac{1}{n_y^2}; \Big(\frac{1}{n^2}\Big)_3\Big|_{E_0=0} = \frac{1}{n_z^2}, \tag{2.35}$$

and the mixed terms are

$$\Big(\frac{1}{n^2}\Big)_4\Big|_{E_0=0} = \Big(\frac{1}{n^2}\Big)_5\Big|_{E_0=0} = \Big(\frac{1}{n^2}\Big)_6\Big|_{E_0=0} = 0. \tag{2.36}$$

The linear changes in the coefficients $(\frac{1}{n^2})_i$, with $i = 1 \ldots 6$, induced by the applied electric field $E_0(E_x, E_y, E_z)$ can be rewritten as

$$\Delta\Big(\frac{1}{n^2}\Big)_i = \sum_{j-1}^{3} r_{ij}E_j, \tag{2.37}$$

where $i = 1 \ldots 6$ and $j = 1 \ldots 3$ and denotes the projections of the applied field $E_0$. The only non-zero coefficient of the electro-optic tensor, i.e. $r_{ij}$, for a cubic crystal such as ZnTe is $r_{41}$ [40]. To calculate how an electromagnetic wave changes when propagating through an electro-optic material in the presence of an applied electric field, it is necessary to transform the deformed refractive index ellipsoid (eq.2.34) to the principal axes of the original ellipsoid (eq.2.33). The deformed ellipsoid will then contain the original indices $n_x, n_y, n_z\big|_{E_0=0}$, but not the mixed terms. Now the deformed ellipsoid will only depend on $n_x, n_y, n_z\big|_{E_0}$, $E_1, E_2, E_3$ and the electro-optic tensor $r_{ij}$.

The following calculations will show how the refractive index changes in an <110> oriented ZnTe crystal with a thickness $d$. Without an external applied electric field, the refractive indices $n_{x,y,z} = n_0$ are equal in all three directions $x_0, y_0$ and $z_0$. In the case where the electric field $E_0$ is oriented parallel to the $z_0$ crystal axis, according to eq.2.33 and eq.2.37, the deformed index ellipsoid will have the form

$$\frac{x^2}{n_0^2} + \frac{y^2}{n_0^2} + \frac{z^2}{n_0^2} + 2r_{41}E_0xy = 1 \tag{2.38}$$

The result of an applied electric field is no transformation in the axis $z = z_0$, and with a rotation of 45° of the x and y axes around z gives the following refractive index along the new axes:

$$\begin{aligned} n_x &\approx n_0 + \frac{1}{2}n_0^3 r_{41}E_0, \\ n_y &\approx n_0 - \frac{1}{2}n_0^3 r_{41}E_0, \\ n_z &= n_0. \end{aligned} \tag{2.39}$$

If we now send a plane electromagnetic wave normal to the crystal surface and polarized 45° with respect to the z axis. This wave will only interact with the x and z components of the refractive index $n_x$ and $n_z$, which are different from each other, since the polarization of the electromagnetic wave has 0 projection on the y axis. Because the x and z components of the incident electromagnetic wave will propagate through the crystal with different velocities, the wave will experience a *phase retardation*. This phase difference can be written as

$$\Delta\phi = \frac{\omega(n_x - n_z)d}{c} = \frac{1}{2}\frac{\omega n_0^3 r_{41}E_0 d}{c}, \tag{2.40}$$

where $\omega$ is the angular frequency of the incident electromagnetic wave. One of the most commonly used methods for the detection of the THz transients is to measure this phase retardation in the non-linear crystals, which is induced by low-frequency electric fields.

# Chapter 3

# THz Time-domain spectroscopy

## 3.1 Ultrafast lasers and a femtosecond Ti:Sapphire amplifier system

The term *Ultrafast lasers* is often used for mode-locked lasers emitting ultrashort pulses. Femtosecond lasers belong to this category.

A common technique for generating pulses with such short pulses is called mode-locking. A mode-locked laser uses the technique of active- or passive mode-locking, so that a periodic train of ultrashort pulses are emitted. Active mode-locking involves the use of a modulator to synchronize the round trips, see 3.1a. The pulse duration of active mode-locked lasers is typically in the picosecond regime. Passive mode-locking involves a saturable absorber, an optical component with a certain optical loss which is reduced at high intensities. See Figure 3.1b. Since the saturable absorber is driven by short pulses, it can modulate the resonator losses much faster than a modulator. This result in shorter pulses and a passive mode-locked laser is typically in the femtosecond regime.


(a) Active mode-locking.

(b) Passive mode-locking.

Figure 3.1: Principles of active mode-locking and passive mode-locking [17].

The pulses can be many orders of magnitude shorter than its cavity round-trip. This is done by simultaneous lasing of multiple longitudinal modes where all modes have a fixed mode spacing and a fixed phase relationship with each other [17]. This forms a stationary waveform in time and space. Each time the pulse hits the output coupler mirror, a usable pulse is emitted so that a pulse train leaves the laser. These lasers require a gain medium with a large gain bandwidth. Short pulses have very broad spectra. Most of the mode-locked lasers are continuously pumped, usually with a laser diode which supplies energy to the gain medium. The circulating pulse can then extract energy in regular time intervals which emits light.

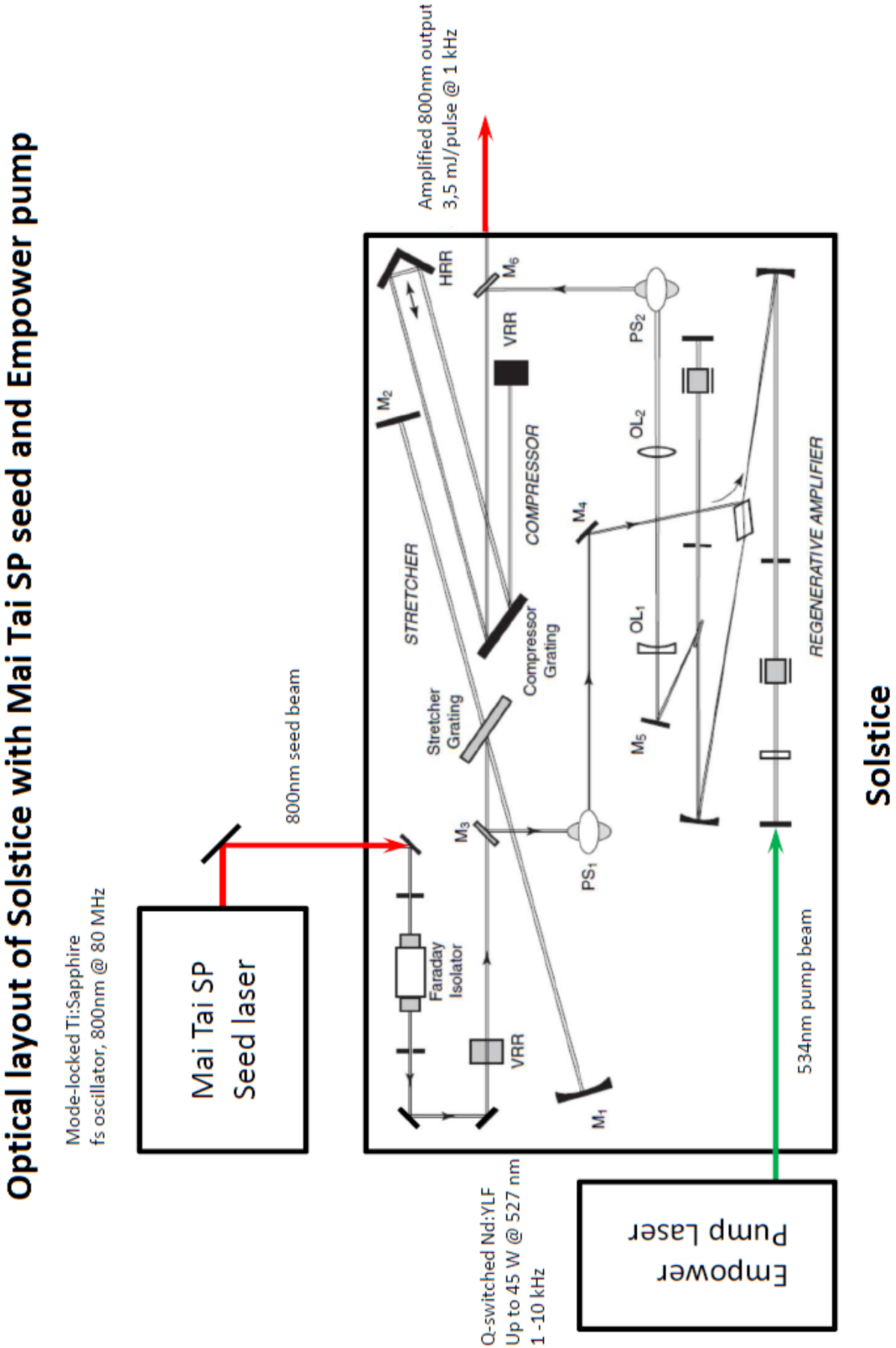


Figure 3.2: A schematic of Solstice Ti:Sapphire amplifier system from Newport Corporation.

A setup driven by a commercial femtosecond Ti:Sapphire amplifier laser (Solstice, Newport Corporation) has been used in this work to perform the THz time-domain spectroscopy experiments (specifications found from [8] and Solstice user manuals). A schematic of this system is depicted in figure 3.2 and consists of five main parts: a seeding laser (Mai Tai), a pump laser (Empower), a stretcher, a compressor and a regenerative amplifier.

The Mai Tai is made up by two parts: The first one is a continuous wave (CW) diode-pumped laser which produces the ultrafast seed pulses for amplification, with an average output power of 1.1 W and a wavelength of 798 nm (half of the power of the Mai Tai is available separately as emission from a port on the front of the Solstice amplifier). The second part is a mode-locked Ti:Sapphire resonator which consists of a Ti:Sapphire rod, focusing mirrors and other optics. The Mai Tai is capable of delivering a tunable pulsed power output at 80 MHz repetition rate with a range of wavelengths from 790 to 810 nm. The CW pump laser is based on the Spectra-Physics *Millenia* diode-pump laser and the mode-locked Ti:Sapphire laser is based on the Spectra-Physics *Tsunami* femtosecond (fs) pulsed laser.

The Empower pump laser is an intracavity-doubled, Q-switched, frequency-doubled, diode-pumped Nd:YLF laser that produces a green pulsed 527 nm beam, used to provide the optical energy to amplify the pulses. The heart of the Empower is a rod of neodymium-doped yttrium lithium fluoride (Nd:YLF) and an array of diode lasers which pumps the Nd:YLF rod to excite neodymium atoms at a wavelength of 1053 nm. This 1053 nm light is frequency-doubled to 527 nm green light and emitted as energetic Q-switched pulses. Q-switching is a mean of concentrating the continuous optical output into a series of brief, high-powered pulses. These pulses are used to pump the regenerative amplifier, which amplifies the mode-locked seed pulses from the Mai Tai.

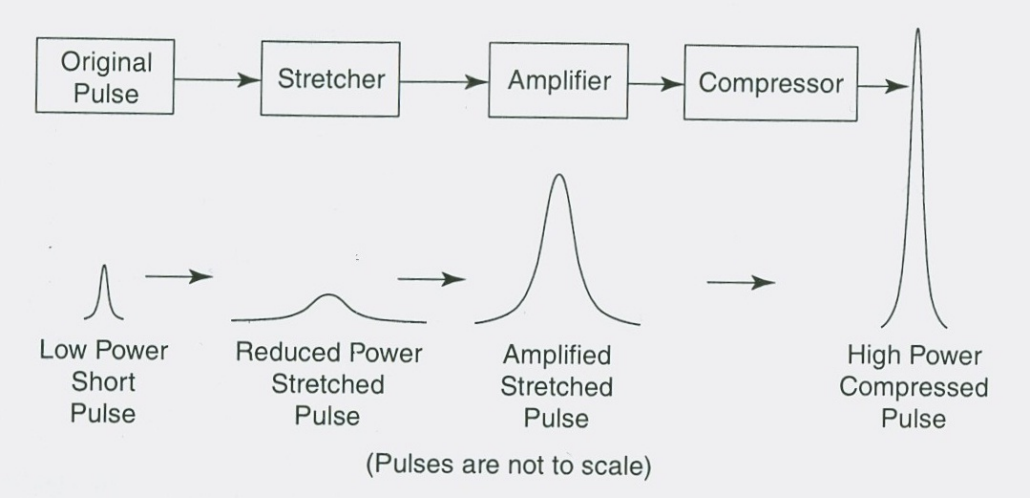


Figure 3.3: A schematic of a pulse stretcher.

To prevent any damage to the amplifier crystal because of the high intensities from the laser pulses, a grating-based pulse stretcher is used to decrease the peak intensity. The phenomenon of delaying or advancing some wavelengths relative to others is called Group Velocity Dispersion (GVD), or less formally "chirp", which is the technique used for stretching a very short seed pulse to increase its duration and hence reduce its peak power. The stretcher chirps the 100 fs transform-limited oscillator pulse and can lengthen the pulse by as much as $10^4$ by using a

combination of dispersive optics to form a "pulse stretcher". Figure 3.3 shows a simplified pulse stretcher where a short pulse is spectrally spread, by making one end of the spread pulse travel farther than the other end, which result in a temporally broadened pulse. The same optical components used in the stretcher can act as a compressor to reverse the process.

The Ti:Sapphire regenerative amplifier, which is pumped by the Empower laser with pulses with a repetition rate of 1 kHz, is designed to amplify individual pulses from a mode-locked Ti:Sapphire laser. When the Ti:Sapphire is excited by the pump pulses, it turns into a gain medium for a short period of time. The regenerative amplifier contains synchronized Pockels cells to let in the train of mode-locked seed pulses from the stretcher. The result of this is that only one stretched pulse can enter the amplifier in a period of 1 ms. The stretched pulse gains energy from the excited Ti:Sapphire amplifier crystal. When it is amplified, the synchronized Pockels cell lets it out and into the compressor.

The last main part of the system is a grating-based pulse compressor. The compressor "restores" the amplified stretched pulse back into a 100 fs transform-limited pulse by giving it a negative chirp, using similar technique as for the stretcher. The output of the system used in this work has a transform-limited pulse with a continuous-wave average power ($P_{ave}$) of 3.5W, an energy of $3.5\frac{mJ}{pulse}$, a wavelength of $\sim$ 800 nm, diameter of 7 mm and a repetition rate ($T_{rep}$) of 1 kHz.

Calculations for finding the pulse width ($\Delta t_p$), peak power ($P_{peak}$) and intensity of this laser system can be done by using an auto-correlator. The auto-correlator is an instrument that displays the temporal pulse and calculates the full-width-half-maximum (FWHM) continuously, shown in figure 3.4. For instructions on how to use the auto-correlator, see Appendix B.

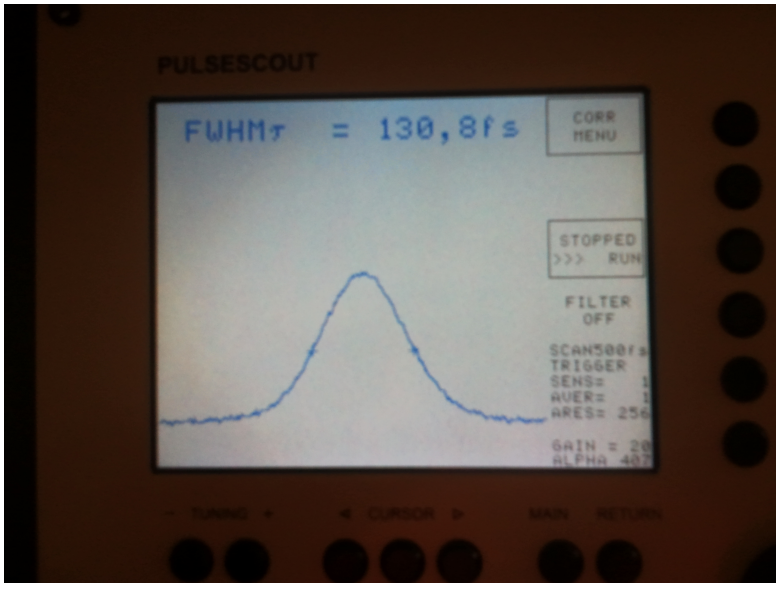


Figure 3.4: A picture of the auto-correlator displaying the FWHM of the laser pulse.

As seen from figure 3.4, the FWHM of this system is 130 fs. The pulse is a $sech^2$, which means that the FWHM has to be multiplied by 0.65 to find the width of the pulse. From the following equations one can find the width and peak power of the pulse.

$$\Delta t_{pulse} = 0,65 \cdot 130fs = 85fs \tag{3.1}$$

$$P_{avg} \cdot \Delta t_{rep} = P_{peak} \cdot \Delta t_{pulse} \tag{3.2}$$

$$P_{peak} = \frac{3,5W \cdot 10^{-3}s}{85 \cdot 10^{-15}s} = 41,2GW \tag{3.3}$$

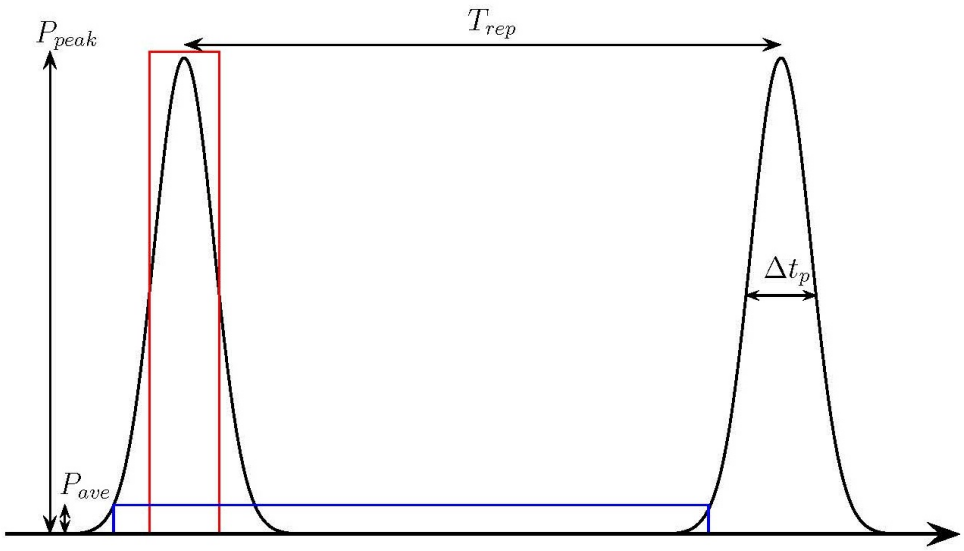


Figure 3.5: An illustration of $P_{peak}$, $P_{ave}$, $\Delta t_p$ and $T_{rep}$.

The diameter of the pulse is given by the manufacturer to be $d = 0.7$ cm. To find the intensity of the pulse we divide the peak power by the area of the beam.

$$A = \frac{\pi \cdot d^2}{4}cm^2 = \frac{\pi \cdot 0,7^2}{4} = 0,385cm^2 \tag{3.4}$$

$$I = \frac{P_{peak}}{A} = \frac{41,2GW}{0,385cm^2} = 107\frac{GW}{cm^2} \tag{3.5}$$

The peak power and pulse intensity of this system were found to be 41.2 GW and $107\frac{GW}{cm^2}$.

## 3.2 Lock-in amplifier

To improve the signal-to-noise ratio (SNR) of the THz-TDS setup in this work, which will be explained in chapter 4, the combination of a lock-in amplifier and a chopper was used. A lock-in amplifier is an instrument used to measure and extract signals buried in a noisy environment. It is also used to provide high-resolution measurements of clean signals because it can detect and measure signals over a large order of magnitude and frequencies, even very small signals all the way down to the scale of a few nanovolts.

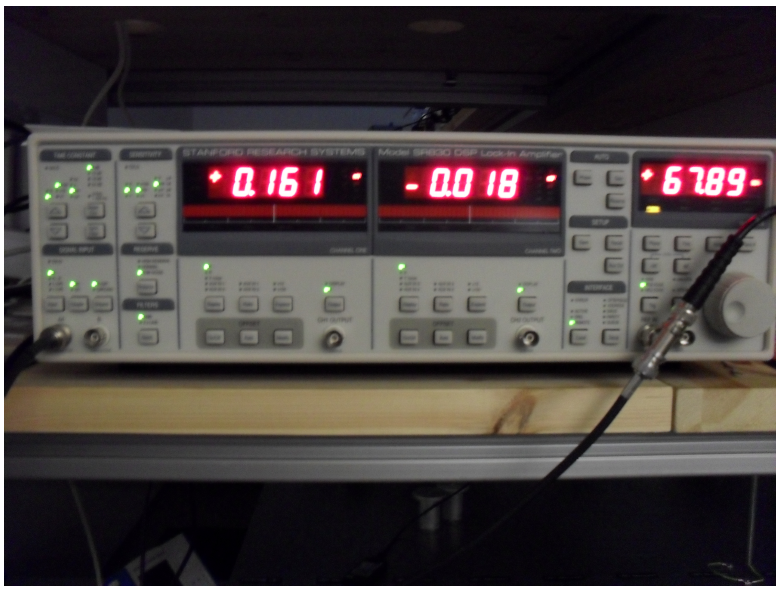


Figure 3.6: A picture of the display and front panel of the lock-in amplifier.

A picture of a lock-in amplifier is shown in Figure 3.6. The lock-in amplifier uses a phase-sensitive detector (PSD), which is the heart of the instrument, to detect the desired signal at a specific reference frequency and phase. The PSD is a demodulator or mixer which operates by multiplying two signals together [2]. It works by having a reference signal "locked" to it to determine the signal you are looking for by comparing the phase and the frequency. This is done by a phase-locked loop that locks the external signal so that it generates its own reference signal. The reference signal allows for extremely small bandwidths to be defined for the purpose of improving signal-to-noise ratio, hence find the desired signal [1]. The output of PSD is a product of two sine waves, derived in equation 3.6 - 3.9 [1]. A schematic of a lock-in amplifier can be seen in Figure 3.7.

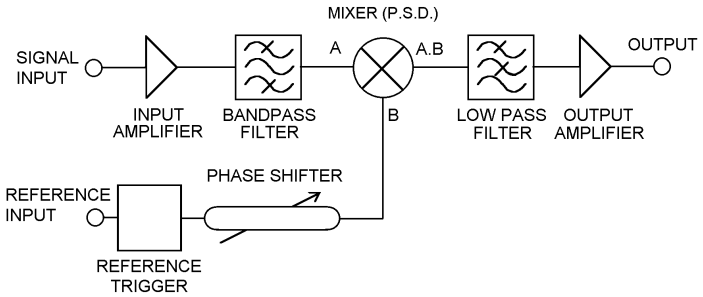


Figure 3.7: A schematic of the principles a lock-in amplifier is built upon [2].

$$\begin{aligned} V_{psd} &= V_{sig} \times V_{ref} \times sin(\omega_{sig}t + \theta_{sig} \times sin(\omega_{ref}t + \theta_{ref}) \\ &= \frac{1}{2} \times V_{sig} \times V_{ref} \times cos((\omega_{sig} - \omega_{ref}) + \theta_{sig} - \theta_{ref}) \\ &- \frac{1}{2} \times V_{sig} \times V_{ref} \times cos((\omega_{sig} + \omega_{ref}) + \theta_{sig} + \theta_{ref}). \end{aligned} \tag{3.6}$$

If the output signal is passed through a low-pass filter, the AC signals are removed and generally nothing is left. The noise at frequencies nearby the carrier frequency will be signals with low

frequencies and thereby filtered out by the low-pass filter. Further analysis from the formula shows that if the frequencies are equal to each other ($\omega_{sig} = \omega_{ref}$), we see that the output of the PSD is a DC signal proportional to the signal amplitude [1].

$$V_{psd1} = \frac{1}{2} \times V_{sig} \times V_{ref} \times cos(\theta_{sig} - \theta_{ref}). \tag{3.7}$$

Since we can adjust the reference level, we can set $\theta = \theta_{sig} - \theta_{ref}$ equal to zero. This is shown in Figure 3.8a. If $\theta$ is 90° we get no signal at all, but this can be eliminated by adding another PSD signal which has a reference signal with a phase-shift of 90°. See Figure 3.8b.

$$V_{psd2} = \frac{1}{2} \times V_{sig} \times V_{ref} \times sin(\theta_{sig} - \theta_{ref}). \tag{3.8}$$

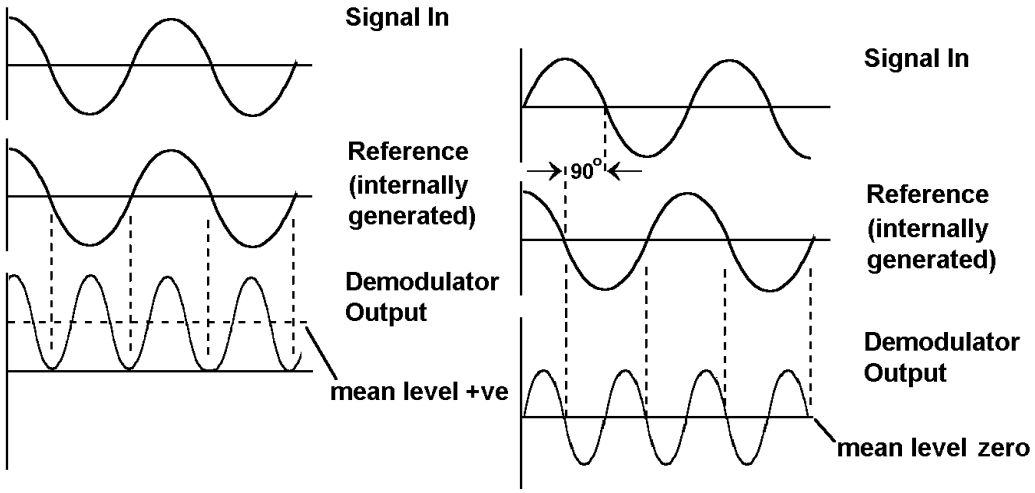


(a) Signal in-phase. (b) Signal out-of-phase.

Figure 3.8: Signal in-phase and out-of-phase [2].

By computing these two signals we find the magnitude of the signal, which also eliminates the phase dependency.

$$V_{psd} = (V_{psd1}^2 + V_{psd2}^2)^{\frac{1}{2}} = V_{sig}. \tag{3.9}$$

By having a dual phase sensitive detection with reference signals 90° apart, the signal can be measured directly. This is called a dual-phase lock-in amplifier, and is by far the most common used lock-in amplifier because; If the phase of the signal changes, it will not affect the magnitude of the output signal. Modern lock-in amplifiers offers some additional functions than the ones already described, such as [1]:

- An AC signal recovery instrument
- A phase meter
- A noise measurement unit
- A vector voltmeter
- A spectrum analyzer

To understand how to use a lock-in amplifier, see Appendix A. The most important aspect to think about when using a lock-in amplifier is to set the reference signal correctly. Then one can

tune the lock-in amplifier by changing the sensitivity and time-constant to get the best output signal available.

A chopper is introduced in the pump beam to create a good reference signal. The chopper blocks the signal as close to the end of the pulse as possible and removes the noise that arises after the chopped signal. The chopper works in conjunction with a lock-in amplifier to set a reference signal. The narrower bandwidth of the signal, the better signal-to-noise ratio we get and this will also reduce the Johnson-Nyquist noise. The laser used in this experiment has a repetition rate of 1 kHz, which means one laser pulse for every millisecond. The chopper and lock-in amplifier are set to 125 Hz in our experiment which is the same as measuring every eight signal. This is done to have a sufficiently narrow bandwidth to get an acceptable high signal-to-noise ratio and easy to calculate with, but it doesn't need to be exactly 125 Hz. It can also be for instance 100 Hz or 250 Hz, depending on what kind of SNR you want.

Using Figure 3.9 we will attempt to model the chopped signal using Fourier analysis.

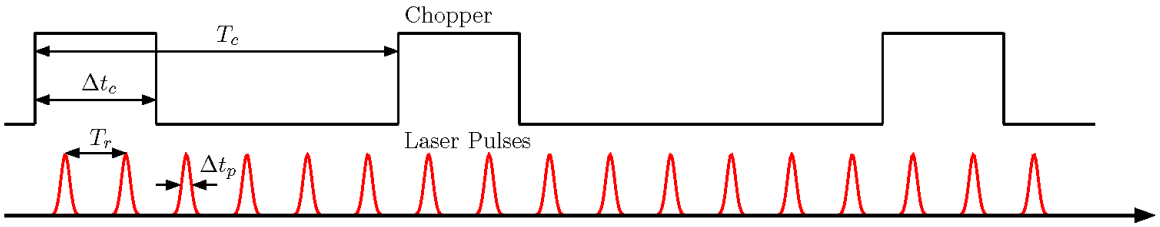


Figure 3.9: Generic timing for chopper.

An essential tool in this analysis is the comb function, $\mathit{III}(t)$, defined as

$$\mathit{III}(t) = \sum_{n=-\infty}^{\infty} \delta(t-n) \tag{3.10}$$

For a pulse train, $p(t)$ with repetition rate $T_r$, we can write it as (ignoring that these are 100fs $sech^2$ pulses and treating them as Dirac delta pulses instead)

$$p(t) = \frac{1}{T_r}\mathit{III}\left(\frac{t}{T_r}\right), \tag{3.11}$$

and it has an accompanying Fourier transform

$$P(\nu) = \mathit{III}(T_r\nu). \tag{3.12}$$

The chopper can be described as a convolution between a rect-function and a comb function, again using Figure 3.9 we obtain

$$chopper(t) = rect\left(\frac{t}{\Delta t_c}\right) * \frac{1}{T_c}\mathit{III}\left(\frac{t}{T_c}\right) = \sum_{n=-\infty}^{\infty} rect\left(\frac{t-nT_c}{\Delta t_c}\right). \tag{3.13}$$

The chopped pulse train, i.e. the signal $s(t)$ seen by the detector, is then mathematically described as

$$s(t) = p(t) \cdot chopper(t). \tag{3.14}$$

This signal, in the frequency-domain, will look like

$$S(\nu) = P(\nu) * Chopper(\nu) = \sum_{n=-\infty}^{\infty} \frac{|\Delta t_c|}{T_r} e^{-i2\pi\nu n T_c} sinc\left(\Delta t_c \nu - \frac{n\Delta t_c}{T_r}\right). \tag{3.15}$$

In the literature there seems to be a confusion over what the optimum chopper frequency is. Zhang's group at Rensselaer Polytechnic advocates a chopper frequency of 125 Hz for a laser with a 1 kHz repetition rate, while the Dutch groups led by Bakker and Woutersen choose a chopper frequency of 500 Hz for the same laser repetition rate. We are not sure why they don't use the pulsed laser at 1 kHz as the reference frequency for the lock-in amplifier in the first place, no chopper needed and shorter data acquisition times. Experiments were performed to find the optimum chopper frequency, which can be found in chapter 4.

## 3.3 THz generation and detection based on ZnTe crystals

The following sections, 3.3.1 and 3.3.2, will give a description of how THz electromagnetic radiation is generated and detected with the use of ZnTe crystals.

### 3.3.1 THz generation

In recent years, many new techniques for generating THz waves have been demonstrated. The two basic techniques for generating THz, solid states and optical generation, were developed in the early $1990's$. Optical generation can be subdivided into photoconduction and optical rectification [6]. In this thesis the method of optical rectification, described in section 2.3, of the 100 fs laser pulses with a central wavelength of $\sim$ 800 nm in a <110>-oriented zinc telluride crystal was used to generate THz waves. ZnTe is a chemical compound and is a semiconductor material with a band gap of 2.23-2.25 eV, it has typically a zincblende structure. It is transparent at the laser pump wavelength at 800 nm, but shows good non-linear properties. At 800 nm wavelength it has a large $2^{nd}$ order non-linear susceptibility $\chi^{(2)} = 1.6 \cdot 10^{-7}$ m/V, and electro-optic coefficient $r_{41} = 4.04$ pm/V [29]. There are several types of non-linear crystals that can be used for generation of THz waves, but ZnTe has been the primary crystal of choice because of its properties.

It is a broadband source of THz radiation via optical rectification and have favourable phase-matching conditions with $\sim$800 nm wavelengths. Since it is nearly transparent in the THz region of the spectrum, allows ZnTe to produce broad-bandwidth pulses in the far-infrared region with large amplitudes. The generation of THz in ZnTe greatly depends on the wavelength of the incoming beam, its intensity and the thickness of the crystal. The orientation of the crystal is also important when it comes to the efficiency of THz emission, therefore an additional experiment was made as seen under section 4.1.2 to optimize the generation efficiency. Experimentalists tend to use thin generation crystals to avoid phase-matching issues. The difference between the

optical group velocity and the terahertz phase velocity will cause a smaller phase difference in thinner crystals, thus limiting the amount of destructive interference. However, a thin crystal is not always the best choice for each application since a decrease in the crystal thickness results in a decrease of the emitted terahertz power [32]. Another drawback for thin crystals is that they can be very fragile, which can complicate commercial applications. Changing the crystal thickness has a large effect on both temporal shape of the terahertz pulse and on its spectrum. By varying the pump wavelength, the oscillation period in the spectrum changes. Experiments on how the crystal thickness and pump wavelength affects the terahertz pulse and the spectrum can be found in reference [32]. From reference [32] and [21], an expression can be derived for the terahertz electric field radiated by optical rectification:

$$E_{Trad}(\omega_T) \sim \omega_T^2 \frac{1 - \exp(-\alpha l_g - i\Delta k_g l_g)}{\alpha + i\Delta k_g}. \tag{3.16}$$

Where $l_g$ is the thickness of the generation crystal, $\alpha$ is the THz absorption coefficient, $\Delta k_g$ is the phase mismatch in the generation crystal and $\omega_T$ is the THz radial frequency. The phase mismatch between the group velocity of the generating pulse and the THz phase velocity determines the amount of destructive interference [32]. The wavelength of the generation beam determines the phase mismatch in the crystal, and therefore the spectra depends on this wavelength.

An electromagnetic pulse with a frequency spectrum in the THz range is produced by the 100 fs laser pulse with a wavelength of $\sim 800$ nm, which excites a transient non-linear polarization spike in the ZnTe emitter crystal. This process is described by the equations 2.17, 2.18 and 2.29 in section 2.1 and 2.3. As explained under section 2.3, optical rectification can be understood as the difference frequency analogue of second harmonic generation. A wave mixing between two frequencies, $\omega_1$ and $\omega_2$, occurs when light interacts with a non-linear medium [21]. The result of this wave mixing, given by equation 2.28, is the sum-frequency generation, $\omega_1 + \omega_2$, and difference frequency generation, $\omega_1 - \omega_2$. When $\omega_1 = \omega_2$, both second harmonic and DC pulses are generated. The "DC" pulse corresponds to the envelope of the optical generated pulse rather than a constant DC level since the near-IR pulse has a duration of 100 fs. This "DC" pulse has to be taken into consideration when doing the data analysis described in section 3.5. In the case of difference frequency mixing, a low frequency polarization is produced which follows the envelope of the incident pulse. The non-linear polarization in the time-domain can be expressed as:

$$P_i^{(2)}(t) = \chi_{ijk}^{(2)} E_j(t) E_k(t). \tag{3.17}$$

From eq. 3.17 one can see that the polarization is proportional to the intensity of the optical generated pulse and the second-order non-linear susceptibility. This polarization moves with the group velocity of the optical pulse and the contribution from the infrared lattice vibration of the low-frequency dielectric response results in a faster velocity for the source than for the radiation, which restricts the bandwidth for efficient phase matching. When the phase of the THz wave travels at the same speed as the optical pulse envelope, phase matching is achieved. The accumulated group velocity mismatch between the optical pulse and the THz that have co-propagated through a material of thickness $d$ can be expressed as [24] [29]:

$$\delta(\omega_{THz}) \approx \frac{[n_g(\lambda_{opt}) - n(\omega_{THz})]d}{c}, \tag{3.18}$$

where $\lambda_{opt}$ is the wavelength of the optical pulse, $n_g(\lambda_{opt})$ is the optical group index and $n(\omega_{THz})$ is the THz phase index. From reference [9] we get that the optical-to-THz conversion efficiency, $\eta_{THz}^{PW}$, in the process of optical rectification is:

$$\eta_{THz}^{PW} = \frac{\sqrt{2} d_{eff}^2 E_0^2}{n_\nu n_{THz} \Delta n^2 \tau} \cdot [1 - \exp^{(\frac{-\Delta n^2 L^2}{c^2 \tau^2})}]. \tag{3.19}$$

Processes such as second harmonic generation (SHG), two-photon absorption (TPA) and free-carrier absorption (FCA) compete with optical rectification. SHG removes photons from the excitation pulse that would normally produce THz radiation and TPA depletes the excitation beam intended for optical rectification and produce free-carriers. These free-carriers can absorb the generated THz radiation through FCA [15]. FCA attenuates the latter part of the terahertz pulse and TPA depletes the available power for terahertz generation. These processes become problematic for high excitation intensities and reduce the THz generation efficiency. A limiting factor for the use of ZnTe for THz generation is that is has a broad TA-phonon absorption line at 1.7 and 3.7 THz in addition to a TO-phonon resonance at 5.3 THz, which limits the bandwidth to below 5 THz [37] [12].

One of the advantages by using optical rectification for generating THz waves is that it is a non-resonant method and the THz pulse width is not limited by the response time of the material, only by the optical laser pulse width and the phonon-mode absorption of the crystal. Bandwidths up to 100 THz have been generated in this way, by choosing the appropriate nonlinear medium and optical generating pulse length it is possible to tune the generated radiation bandwidth between 2.5 THz and 100 THz [3].

### 3.3.2 THz detection

The generation of THz waves is pointless without an effective way of detection. There are several ways to detect THz waves and the two primary optoelectronic methods for detection are photoconductive antennas and free-space electro-optic sampling (FSEOS). In the setup for this thesis, free-space electro-optic sampling is used for detecting THz pulses. One of the advantages of FSEOS is that it is a non-resonant method of detection, so the potential for damaging the detector crystal is much lower [29]. Electro-optic THz receivers have demonstrated exceptionally high-frequency performance, but have not demonstrated the continuous spectral coverage of photoconductive antennas. This is due to THz absorption and dispersion of the EO crystal, the frequency dependence of the EO susceptibility and phase mismatch between the interrogating pulse and the THz pulse [11]. Electro-optic detection is an increasingly popular way to measure the amplitude and phase of THz radiation. There are two reasons for this: First, unlike time-gated antennas, electro-optic materials are readily commercially available. Second, electro-optic detection is suitable for signals with a large bandwidth [26].

Free-space electro-optic sampling is based on the electric field of a THz pulse, which through a non-linearity of the first order (Pockels effect) induces a small birefringence in the electro-optic crystal. A weak 800 nm laser pulse is used as a probe, co-propagating with the THz pulse through the crystal. The result of this effect is that the initially linearly polarized optical probe beam gains a small elliptical polarization when propagating through the electro-optic crystal, where the ellipticity the probe beam experience is proportional to the electric field applied to

the crystal. The electric field of THz radiation that the probe pulse experience can be approximated as a DC bias field since the THz pulse is much longer than the probe pulse ($\sim$ 1 ps vs. $\sim$ 100 fs), and the whole time profile of the THz pulse can therefore be traced by measuring the phase retardation (see eq. 2.40) using a variable delay line (VDL) to temporally delay the probe with respect to the pump. The width of the THz detection probe pulse and the step length of the VDL determines the temporal resolution.

Crystals with zincblende structure such as ZnTe and GaP are often used for electro-optic detection. ZnTe is very suitable because its refractive index in the far-IR and near-IR are comparable, which results in efficient THz detection [26]. The efficiency of the ZnTe detection crystal can be optimized by rotating the azimuthal angle of the crystal, same as for the generation crystal. Experiments on the angle of the detection crystal can be found under section 4.1.2. A thicker detection crystal will increase the sensitivity of the system because of the length of the interaction between the field and electro-optic probe is increased [6].

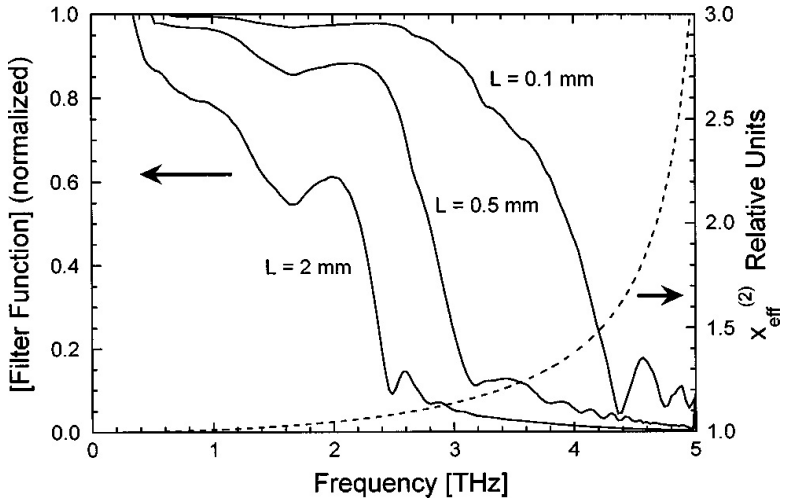


Figure 3.10: Calculated $\chi^2_{eff}$ (dashed line) shown on a relative scale (right ordinate). Calculated and normalized to the unity (left ordinate) filter function, shown as the solid lines, using the measured absorption and index of refratcion for ZnTe and the indicate crystal thickness of $L = 0.1$ mm, $L = 0.5$ mm and $L = 2$ mm [12].

As seen from figure 3.10, how far into the THz region it is possible to detect with ZnTe strongly depends on the thickness of the detection crystal. The figure shows the frequency dependence of $\chi^2_{eff}$ from low frequencies up to 5 THz. There is a broad TO-phonon line at 1.7 THz and much stronger lines at 3.7 THz and 5.3 THz [12]. Even though increasing the crystal length will increase the sensitivity of the system, increasing the length will also increase the effects of phase mismatch and absorption. These effects will reduce the effective bandwidth of the EO detection process. A summary of reference [12] gives that EO detection with ZnTe below the TO-phonon resonance at 5.3 THz, the useful frequency range is limited by the crystal properties.

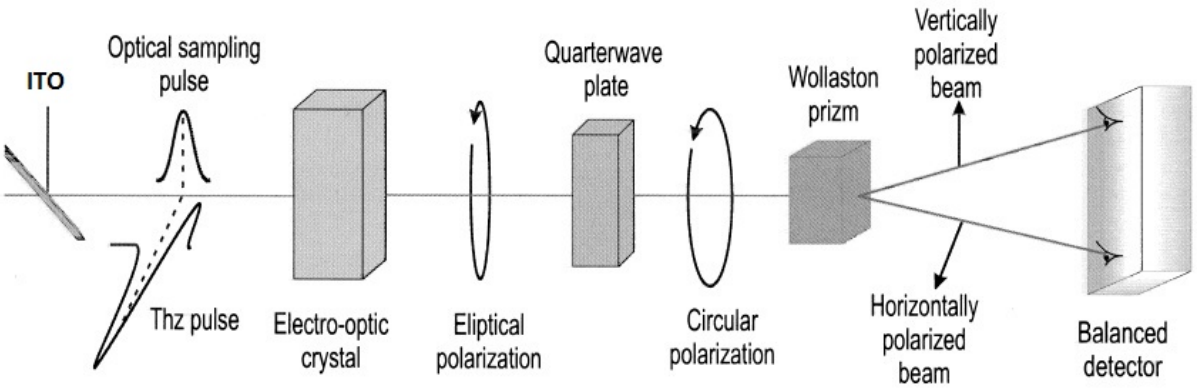


Figure 3.11: A schematic of free-space electro-optic sampling detection. ITO - Indium Tin Oxide [29].

Electro-optic detection is in practice, see figure 3.11, done by having a quarter-wave plate ($\frac{\lambda}{4}$) behind the electro-optic crystal to make the initially linear polarization of the probe beam circular when there is no applied electric field, i.e. $E_{THz} = 0$. A Wollaston prism then separates the beam into two components and sends them to a differential detector, consisting of two photodiodes (PD A and PD B). In the absence of THz, the two components have equal intensity and the differential signal between PD A and PD B is zero. When a THz wave and the probe beam interacts in the non-linear crystal, the birefringence caused by the applied electric field will result in a phase retardation of the optical probe pulse and it will become elliptically polarized. This will result in different light intensities incident on PD A and PD B. PD A and PD B will will then produce a difference in voltages which will be proportional to the induced phase retardation and according to eq. 2.40, proportional to the electric field strength of the THz pulse. This difference is not only proportional to the magnitude of the applied electric field, but also its sign which makes the whole detection method phase-sensitive as well. In other words, this detection method can measure both the amplitude and the phase of the applied electric field. Calculations for the applied electric field can be found under section 3.5.2.

## 3.4 Theory and setup of a THz time-domain spectroscopy system

Optical generation and coherent detection of terahertz pulses have found extensive application to spectroscopy in a frequency region that is difficult to reach by other means. The measurement method used in this thesis is terahertz time-domain spectroscopy (THz-TDS). All the measurements are done in the time-domain, where the electric field of the THz pulse is measured as a function of time. THz-TDS uses a single ultrashort pulse (typically femtoseconds) to generate a THz pulse, which can then be detected. A key advantage of the THz-TDS is that one can fully describe the dielectric properties of a sample material, since one are able to measure both the amplitude and the phase of the electric field of the THz pulses. There are several methods for both generation and detection of the THz radiation, which are discussed in section 2.3 and 2.4. The methods used in this thesis are optical rectification for generation of THz, and free-space electro-optic sampling (FSEOS) for detection.

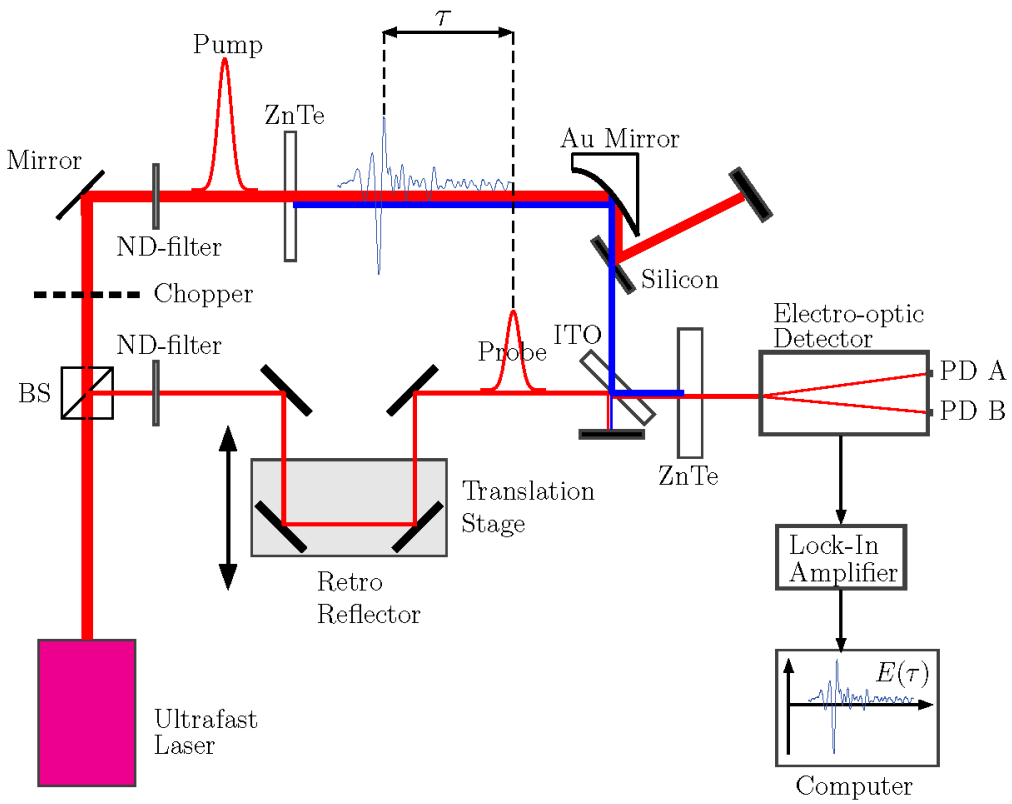


Figure 3.12: A schematic of the THz-TDS system. The red lines are 800 nm light and the blue line is the THz radiation which gets focused by the paraboloidal gold (Au) mirror.

The basic ideas and setup of the THz-TDS system in this thesis using optical rectification and FSEOS is illustrated in figure 3.12. The initial laser beam goes through a beam sampler which separates the beam into two, where the two will be the probe and the pump beam. A neutral density (ND) filter is used as an attenuator for the probe beam to decrease its intensity, so that the intensity does not exceed the damage threshold of the electro-optic detector. A variable delay line (VDL) is introduced, mounted with a retro-reflector, to delay the probe pulse in time with respect to the THz pulse.

$$\tau = \frac{2 \cdot \Delta L}{c}. \tag{3.20}$$

| Variable delay line [L] | Time-delay [$\tau$] |
|---|---|
| 1 mm | 6.67 ps |
| 0.1 mm | 667 fs |
| 0.01 mm | 66.7 fs |
| 0.001 mm | 6.67 fs |

Table 3.1: Translation stage's step length related to the delay in time.

The formula for the time-delay is given by equation 3.20. Where $\tau$ is the time-delay, $\Delta$L is the distance the VDL is moved and c is the speed of light. The multiplication by 2 comes from the fact that the beam has to travel both back and forth through the retro reflector. The temporal resolution is given by the step length of the VDL. Smaller step lengths results in a

better temporal resolution of the experiments. To get a better understanding of this equation and the temporal resolution, see table 3.1.

The pump beam on the other hand is where the THz is generated by optical rectification in a non-linear crystal, i.e. a 2 mm thick ZnTe crystal. The damage threshold of ZnTe is $\sim 100\frac{GW}{cm^2}$, so the intensity of the pump beam was kept far below this threshold for our experiments. For the setup showed in figure 3.12, an intensity of $1\frac{GW}{cm^2}$ was used. A paraboloidal gold mirror is introduced to guide and focus the THz radiation. Somewhere along this beam path, a chopper (Model SR540) is needed to set the reference signal for the lock-in amplifier (see section 3.2) and is set to 125 Hz in this setup. Further along the beam path of the THz wave, a thin sample of silicon is used to get rid of the remaining 800 nm light. Silicon reflects 800 nm light by almost 99%, but only has a transmission of THz of 55%. This means that there is a loss of THz radiation by 45% when using silicon for this purpose. An Indium Tin Oxide (ITO) is used to combine and guide the probe and the THz pulse through the detection crystal, i.e. a 1 mm thick ZnTe. How the detection crystal work is described under section 2.4 and 3.3.2. The probe beam is guided into the electro-optic detector (Model Zomega ABL-100), where PD A and PD B are the two balanced photodiodes in the detector. The electro-optic detector is connected to a lock-in amplifier (Model SR830), where the signal is read by a personal computer.

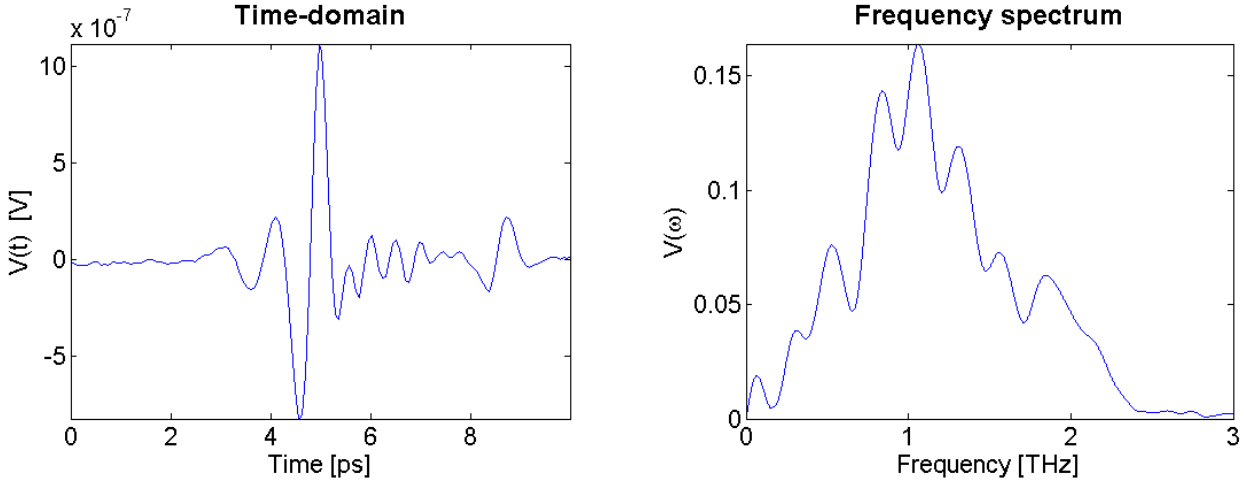


(a) Time-domain.

(b) Frequency-domain.

Figure 3.13: Results obtained from THz-TDS measurements with the setup in figure 3.12.

| Pump power | Probe power | Ref. freq | TC | Sensitivity | Step length | Scan length |
|---|---|---|---|---|---|---|
| 32 mW | $\sim 1$ $\mu$W | 125 Hz | 3 | 100 $\mu$V | 0.01 mm | 1.5 mm |

Table 3.2: Measurement settings for figure 3.13. Ref. freq and TC are abbreviations for reference frequency and time-constant used for the lock-in amplifier.

A typical THz pulse and its frequency spectrum can be seen in figure 3.13a and 3.13b, obtained from the setup used in figure 3.12. Later in this thesis, chapter 4, possibilities for improving this setup will be explored.

To perform a THz-TDS experiment, a sample of the material has to be placed along the THz beam path. For the setup used in this thesis, it has to be placed between the thin silicon sample

used for blocking the 800 nm light and the ITO used for combining the two beams. A pulse with THz-frequency electromagnetic radiation passes through this sample and its profile is compared to a reference pulse [36]. The measurements are done by recording the interaction of the THz wave with the sample and measure the waveform of the THz wave. The recordings are snapshots of the THz pulse as it is delayed by the VDL with respect to the probe pulse. When the THz wave passes through the material, it can change the amplitude or the shape of the pulse. It can also delay the pulse or have other effects such as scattering. A Fourier transformation (FT) is applied on the acquired data to get the frequency spectrum of the detected signal. Since it is the electric field that is measured instead of the intensity, it provides information of both the amplitude and the phase of the detected signal. It is by comparing the frequency spectrum of the reference signal and the signal through a material that one can calculate the absorption coefficient and the refractive index of the material [7]. The absorption coefficient and the refractive index are frequency dependent, as will be shown later in this thesis. Since the pump and the probe laser pulses is derived from the same laser beam, a fundamental limitation of the THz-TDS is that it is not possible to measure THz pulses shorter than the probe pulse itself. Hence the bandwidth of the THz pulse cannot exceed that of the probe pulse [29].

The refractive index, $n$, is defined as the factor by which the wavelength and the velocity of the radiation are reduced with respect to their vacuum values. Electromagnetic waves phase velocity is slowed in a material, i.e. the refractive index of the materials used in the THz-TDS setup has to be considered when calculating the optical length that the probe beam and the THz beam travels to find where the two beams interacts with each other. Its most elementary occurrence is in Snell's law of refraction. Absorption of electromagnetic radiation is the way by which energy of a photon is taken up by matter and the absorption of light is often called attenuation. It is a gradually loss in intensity of flux through a medium. How easily a material or medium can be penetrated by a beam of light is often characterized as a quantity by the absorption coefficient, $\alpha$. It is measured using units of reciprocal length, usually in $cm^{-1}$. A medium with large absorption coefficient means that the intensity of the beam is quickly reduced when passing through, and a small absorption coefficient means that the medium is relatively transparent to the beam. Water vapour was the first molecule to be measured by THz-TDS. Water has a strong absorption in many of the frequency bands in the THz range. High water content in a sample or high relative humidity of the environment would therefore greatly affect the frequency spectrum at certain frequencies. A dry nitrogen ($N_2$) or vacuum environment could be used to reduce the water absorption of the THz wave. Experiments were performed with and without $N_2$ to see the effects of water molecules in the air and reduce the absorption. These experiments are found under section 4.1.7.

In a frequency region that has been difficult to reach by other means, spectroscopy obtained by optical generation and coherent detection of terahertz pulses have found many promising areas of applications. THz-TDS is preferred over X-rays for applications such as identification of materials or polymorph identification because terahertz radiation is non-ionizing radiation and does not cause any health hazards. The spectroscopic information obtained by THz-TDS combined with imaging techniques have a high potential in many areas of applications such as biochemical, drug screening, medical diagnostics and detection of explosives. One of the most prominent advantage of THz imaging is its ability to penetrate a wide range of materials, such as paper, wood, plastics, fabric, ceramics, semiconductors and many others that are opaque in the visible and near-infrared radiation (NIR) [35].

## 3.5 Data analysis

This section will describe how to calculate the absorption coefficient, the refractive index, the electric field strength of the THz radiation, the signal-to-noise ratio and the dynamic range from the acquired data by the use of THz-TDS.

### 3.5.1 Absorption coefficient and refractive index

The calculations for both the absorption coefficient, $\alpha(\omega)$, and the refractive index, $n(\omega)$, are derived from Maxwell's wave equation for an electric field E(z,t). The following equations in this section can be found in reference [14].

$$\frac{\partial^2 \mathbf{E}(z,t)}{\partial z^2} - \frac{1}{c^2}\frac{\partial^2 \mathbf{E}(z,t)}{\partial t^2} = \mu_0 \frac{\partial^2 \mathbf{P}(z,t)}{\partial t^2} + \mu_0 \frac{\partial \mathbf{J}(z,t)}{\partial t}. \tag{3.21}$$

We use a Fourier transformation on the measured temporal signal to transform the signal into the frequency-domain. In the following equations z will be substituted with L ($z = L$).

$$\begin{aligned} Reference : E(0,t), FFT \Rightarrow E(0,\omega) = A(\omega) = E_0' - iE_0''. \\ Sample : E(L,t), FFT \Rightarrow E(L,\omega) = A(\omega)e^{i\frac{\omega}{c}n(\omega)L}e^{-\frac{\alpha(\omega)}{2}L} = E' - iE''. \end{aligned} \tag{3.22}$$

Where $E(0,t)$ is the reference pulse measured without any sample, and $E(L,t)$ is with a sample of thickness L. Once the Fourier transformation has been performed, linear dispersion theory gives

$$E(L,\omega) = E_0(\omega)e^{-ik(\omega)L}, \tag{3.23}$$

where

$$k(\omega)\cdot L = \frac{\omega}{c}n'(\omega)\cdot L - i\frac{\alpha(\omega)}{2}\cdot L = Dispersion - iAbsorption. \tag{3.24}$$

Equation 3.23 can then be rewritten as

$$E(L,\omega) = E_0(\omega)e^{-i\frac{\omega}{c}n'(\omega)L}e^{-\frac{\alpha(\omega)}{2}L}, \tag{3.25}$$

$$\frac{E(0,\omega)}{E(L,\omega)} = e^{\frac{\alpha(\omega)}{2}L}e^{-i\frac{\omega}{c}n(\omega)L} = \frac{E_0' - iE_0''}{E' - iE''} = Re^{i\varphi}, \tag{3.26}$$

where R contains the absorption coefficient.

$$R = e^{\alpha(\omega)L} = \frac{|E_0' - iE_0''|}{|E' - iE''|} = \frac{\sqrt{E_0'^2 + E_0''^2}}{\sqrt{E'^2 + E''^2}} \tag{3.27}$$

The absorption coefficient $\alpha(\omega)$ can then be found by using equation 3.27.

$$\alpha(\omega) = \frac{1}{L} \cdot ln \frac{[E_0'^2 + E_0''^2]}{[E'^2 + E''^2]} \tag{3.28}$$

The refractive index, $n(\omega)$, can be found from $\varphi$ in eq. 3.26.

$$\varphi = \frac{\omega}{c} n(\omega) L = -arctan \left[ \frac{Im\left[\frac{E_0' - iE_0''}{E' - iE''}\right]}{Re\left[\frac{E_0' - iE_0''}{E' - iE''}\right]} \right] \tag{3.29}$$

$$\frac{E_0' - iE_0''}{E' - iE''} = \frac{(E_0' - iE_0'')(E' + iE'')}{E'^2 + E''^2} = \frac{E_0'E' + iE_0'E'' - iE_0''E' + E_0''E'}{E'^2 + E''^2} \tag{3.30}$$

$$Re\left[\frac{E_0' - iE_0''}{E' - iE''}\right] = \frac{E_0'E' + E_0''E''}{E'^2 + E''^2} \tag{3.31}$$

$$Im\left[\frac{E_0' - iE_0''}{E' - iE''}\right] = \frac{E_0'E'' - E_0''E'}{E'^2 + E''^2} \tag{3.32}$$

By inserting the real and imaginary parts in eq. 3.29 we get the dispersion

$$\frac{\omega}{c} n(\omega) L = -\arctan\left[\frac{E_0'E'' - E_0''E'}{E_0'E' + E_0''E''}\right], \tag{3.33}$$

which can be rearranged to get the refractive index $n(\omega)$.

$$n(\omega) = -\frac{c}{\omega L} \cdot \arctan\left[\frac{E_0'E'' - E_0''E'}{E_0'E' + E_0''E''}\right] \tag{3.34}$$

### 3.5.2 Electric field strength

An important aspect of the THz-TDS is that one are able to calculate and measure the electric field strength of the THz radiation. The following equations are found from reference [40]. The incident intensity can be expressed as

$$I_i \propto E \cdot E^* = |E_{x'}(0)|^2 + |E_{y'}(0)|^2 = 2A^2. \tag{3.35}$$

When the output has travelled a distance l, the x' and y' components have acquired a phase shift of $\Gamma$ radians.

$$\begin{aligned} E_{x'}(l) &= Ae^{-i\Gamma}. \\ E_{y'}(0) &= A. \end{aligned} \tag{3.36}$$

The total field emerging from the output polarizer is the sum of y components from eq.3.36.

$$(E_y)_0 = \frac{-A}{\sqrt{2}}(e^{-i\Gamma} - 1). \tag{3.37}$$

This corresponds to an output intensity of

$$I_0 \propto \left[(E_y)_0(E_y^*)_0\right] = \frac{A^2}{2}\left[(e^{-i\Gamma}-1)(e^{i\Gamma}-1)\right] = 2A^2 sin^2\left(\frac{\Gamma}{2}\right). \tag{3.38}$$

The ratio of the output intensity with respect to the input is then

$$\frac{I_o}{I_i} = \frac{2A^2 sin^2(\frac{\Gamma}{2})}{2A^2} = sin^2\left(\frac{\Gamma}{2}\right) = sin^2\left[\left(\frac{\pi}{2}\right)\frac{V}{V_\pi}\right], \tag{3.39}$$

where

$$\begin{aligned} \Gamma &= \frac{\pi}{2} + \Gamma_m sin(\omega_m t), \\ \Gamma_m &= \pi\left(\frac{V_m}{V_\pi}\right), \\ \Gamma_m &= \frac{\omega n_0^3 r_{41} E_{THz} d}{c}. \end{aligned} \tag{3.40}$$

Inserting this into eq.3.39 we get

$$\frac{I_0}{I_i} = sin^2\left(\frac{\pi}{4} + \frac{\Gamma_m}{2} sin(\omega_m t)\right) = \frac{1}{2}\left[1 + sin\left(\Gamma_m sin(\omega_m t)\right)\right]. \tag{3.41}$$

Which for $\Gamma_m \ll 1$ will be

$$\frac{I_0}{I_i} \simeq \frac{1}{2}\left(1 + \Gamma_m sin(\omega_m t)\right). \tag{3.42}$$

Keep in mind that we have two photodiodes, $I_a$ and $I_b$, that can be expressed as

$$\begin{aligned} \frac{I_a}{I_i} &= sin^2\left(\frac{\Gamma}{2}\right), \\ \frac{I_b}{I_i} &= cos^2\left(\frac{\Gamma}{2}\right). \end{aligned} \tag{3.43}$$

The difference in intensity $\Delta I$ is $I_a - I_b$, which with respect to the input intensity is

$$\begin{aligned} \frac{\Delta I}{I_i} = \frac{I_a - I_b}{I_i} &= sin^2\left(\frac{\Gamma}{2}\right) - cos^2\left(\frac{\Gamma}{2}\right) \approx 2sin^2\left(\frac{\Gamma}{2}\right) - 1 \\ &= 2\cdot\left(\frac{1}{2} + \frac{\Gamma_m sin(\omega_m t)}{2}\right) - 1 = \Gamma_m sin(\omega_m t). \end{aligned} \tag{3.44}$$

Since the THz-TDS setup used in this work does not have a modulation voltage $V_m sin(\omega_m t)$ with a modulation frequency $\omega_m$ from an AC source, but uses a THz pulse instead, $sin(\omega_m t) = 1$. Eq. 3.44 can then be expressed as:

$$\frac{\Delta I}{I_i} = \Gamma_m = \frac{\omega n_0^3 r_{41} E_{THz} d}{c}. \tag{3.45}$$

The relation between the intensity and the voltage can be written as follows

$$\begin{aligned} \Delta I &= C \cdot \Delta V, \\ I_i &= C \cdot \frac{V_{max}}{2}, \end{aligned} \tag{3.46}$$

where C is a constant. $\Delta V$ is the difference between the photodiodes, PD A and PD B, in the detector which occurs when $E_{THz}$ is applied. $I_i$ is the input intensity, which is equal to half of the maximum voltage that can be produced from the photodiodes since they are balanced in the absence of $E_{THz}$. The maximum voltage is produced when all the light goes to one PD, and zero to the other. By using eq. 3.45 and eq. 3.46 we get

$$\frac{\Delta I}{I_i} = \frac{C \cdot \Delta V}{C \cdot \frac{V_{max}}{2}} = \frac{2\Delta V}{V_{max}} = \Gamma_m = \frac{\omega n_0^3 r_{41} E_{THz} d}{c}. \tag{3.47}$$

Eq. 3.47 can be rewritten to give the electric field, $E_{THz}$.

$$E_{THz} = \frac{2\Delta V}{V_{max}} \cdot \frac{c}{\omega n_0^3 r_{41} d} \tag{3.48}$$

Where c is the speed of light and $\omega$ is the probe frequency. $n_0$ is the refractive index of the electro-optic crystal, i.e. ZnTe which is $n_0 = 3.22$ [24] for 800 nm. The electro-optic coefficient, $r_{41}$, is $4.04\frac{pm}{V}$ [31] for ZnTe and $d$ is the thickness of the crystal. By inserting the data for the THz-TDS setup in this thesis with a 1 mm crystal, eq. 3.48 can be simplified to

$$\omega = 2\pi \frac{c}{\lambda}, \tag{3.49}$$

$$E_{THz} = \frac{2\Delta V}{V_{max}} \cdot \frac{c}{2\pi \frac{c}{\lambda} n_0^3 r_{41} d} = \frac{\Delta V}{V_{max}} \cdot \frac{\lambda}{\pi n_0^3 r_{41} d}, \tag{3.50}$$

$$\begin{aligned} E_{THz} = \frac{\Delta V}{V_{max}} \cdot \frac{800 \cdot 10^{-9} m}{\pi \cdot (3,22)^3 \cdot 4,04 \cdot 10^{-12} \frac{m}{V} \cdot 10^{-3} m} = \frac{\Delta V}{V_{max}} \cdot 1,89 \cdot 10^6 \frac{V}{m} \\ E_{THz} = \frac{\Delta V}{V_{max}} \cdot 1,89 \cdot 10^4 \frac{V}{cm}. \end{aligned} \tag{3.51}$$

Equation 3.51 will be used to insert the measured data for $\Delta V$ and $V_{max}$ from the THz-TDS experiments. Another way of calculating the electric field, $E_{THz}$, can be found in the reference [26] and [34], but the result is the same.

### 3.5.3 Signal-to-noise ratio and dynamic range

A common practice to describe the performance of a particular TDS system is to quote its dynamic range (DR) and signal-to-noise ratio (SNR). However, there are no commonly agreed standard to our knowledge of calculating the DR and SNR, so there exists many disparate and often contradictory methods of defining these quantities. The values of DR and SNR in the literature are often quoted without mentioning the method of how these values are calculated. A recommendation for best practice for calculations of these values can be found in reference [22], which is the method used in this thesis. For a system like THz-TDS, which measures the amplitude and the phase, the SNR and DR are defined as

$$\text{SNR} = \frac{\text{mean magnitude of amplitude}}{\text{standard deviation of amplitude}}, \tag{3.52}$$

$$\text{DR} = \frac{\text{maximum magnitude of amplitude}}{\text{rms of noise floor}}. \tag{3.53}$$

SNR indicates the minimum detected signal change and the DR describes the maximum quantifiable signal change. For a TDS system one can evaluate the SNR and DR in either with respect to the time-domain or to the frequency-domain calculated by FFT. The standard deviation (SD) varies with the position of the variable delay line (VDL) and is largest where the signal is strongest. A better way to estimate the SNR and DR of the time-domain data is to evaluate the standard deviation (SD) of the peak signal and the noise in the absence of a THz signal. For THz time-domain data, the recommended practice for estimating the DR and SNR is as follows [22]:

1. Measure the time-domain trace and note the value of the peak maximum.

2. Measure the noise signal in the absence of THz, either by blocking the THz signal or use the data before the arrival of the THz pulse.

3. The mean signal in the absence of THz should be constant (zero for electro-optic detection, non-zero for a photoconductive antenna). Calculate its standard deviation.

4. $\text{DR} = \dfrac{\text{mean magnitude of the peak}}{\text{standard deviation of the noise}}$.

5. $\text{SNR} = \dfrac{\text{mean magnitude of the peak}}{\text{standard deviation of the peak}}$.

In this thesis the analysis will be performed on the time-domain data, but a derivation for how to obtain the SNR and DR from the frequency spectrum can be found in the literature [22]. An advantage of this method is that the typically large DR allows for examination of strongly attenuated samples, while the typically lower SNR limits the accuracy and the amplitude resolution. Another important aspect to keep in mind is that optical rectification is a $\chi^{(2)}$ process and photoconductive antennas is a $\chi^{(1)}$ process. This result in measurements obtained by optical rectification have less SNR and DR than that obtained by photoconductive antennas. Free-space electro-optic sampling (FSEOS) is less sensitive compared to photoconducting antenna detectors (PAD), but is free from typical artifacts for PAD like a broad minimum before the main peak and the drifting background. FSEOS is also more mechanically stable than PAD and does not require very precise optical adjustment.

# Chapter 4

# Results and discussion

This chapter will present and discuss the results obtained by the experimental work for this thesis. The setup described under section 3.4 can be significantly improved, as will be explained throughout this chapter. The most significant improvements for the THz-TDS setup will be presented in a subsection for each step. The easiest way to see the effects of the improvements step by step is to examine the temporal profile and the frequency spectrum, and follow the shape and increase in magnitude.

To truly be able to compare the different results with each other, the results had to be normalized since the signal level (actual measured voltage) for the different setups varied. They were normalized by subtracting the voltage level in the absence of THz. The temporal profile was still measured in voltage as a function of time, but normalized so that the $V(t)$ was not the actual measured voltage. Subtracting this voltage level was also important for the frequency spectrum, since it would act as a DC signal. By normalizing the temporal profile we removed the DC level for the frequency spectrum and all that remained was the spectrum for the THz radiation. When comparing the improvements which were done, it is often easier to look at the frequency spectrum since the changes manifests themselves better in this domain. $V(\omega)$ is a normalized value obtained from the Fourier transformation of $V(t)$. The data files were analysed through MATLAB scripts, found in Appendix C.

In the end of this chapter, a brief description and results of some of the applications this setup can be used for will be shown. Measurements performed on semiconductors and wood samples will be presented in this part.

## 4.1 Improvements

### 4.1.1 New setup with ITO windows

To improve the THz-TDS system, a new setup was built. The alignment for the pump and probe beams had to be very precise, especially for the probe beams since it involved the use of a variable delay line (VDL) and a retro reflector. The consequence of a small misalignment of the probe beam prior to the delay line would result in a change of path for the beam as the VDL moved. The beam would then move and enter the electro-optic detector differently, causing the measured signal to have a slope with different voltage levels. These data values wouldn't be fully correlated to the properties of the material and would introduce an error in the subsequent analysis that would distort the end result in such a degree that these results could not be used for further analysis. To avoid any complications of having a paraboloidal mirror, the gold (Au) mirror used in figure 3.12 was replaced with an Indium Tin Oxide (ITO) window. A paraboloidal mirror would focus the THz beam; therefore a second mirror should be used after the focus point with the same distance to the focus point as the first mirror. This would make the beam collinear again. The second mirror often has a small hole in the centre, allowing the probe beam to pass through and then co-propagate along with the THz pulse. At this point we did not have such a mirror to effectively combine these two beams. Since only one gold mirror was used in the first setup, the beam was focused through the sample and into an ITO window to guide the THz beam into the 1 mm ZnTe detection crystal. The gold mirror had a focal length of ∼20 cm, which limited the space available in our setup. The ITO was placed after the 2 mm ZnTe, where the THz was generated, to get rid of some of the 800 nm light which were co-propagating along and to guide the THz wave. ITO has a transmittance of infrared light of 85%, and a reflectance of THz radiation of $80 - 90\%$. Most of the setup remains the same as for figure 3.12, except of the additional ITO window and a neutral density filter for the pump beam. The neutral density filter for the pump beam was needed since the new setup had more intensity because of changes prior to the TDS-setup.

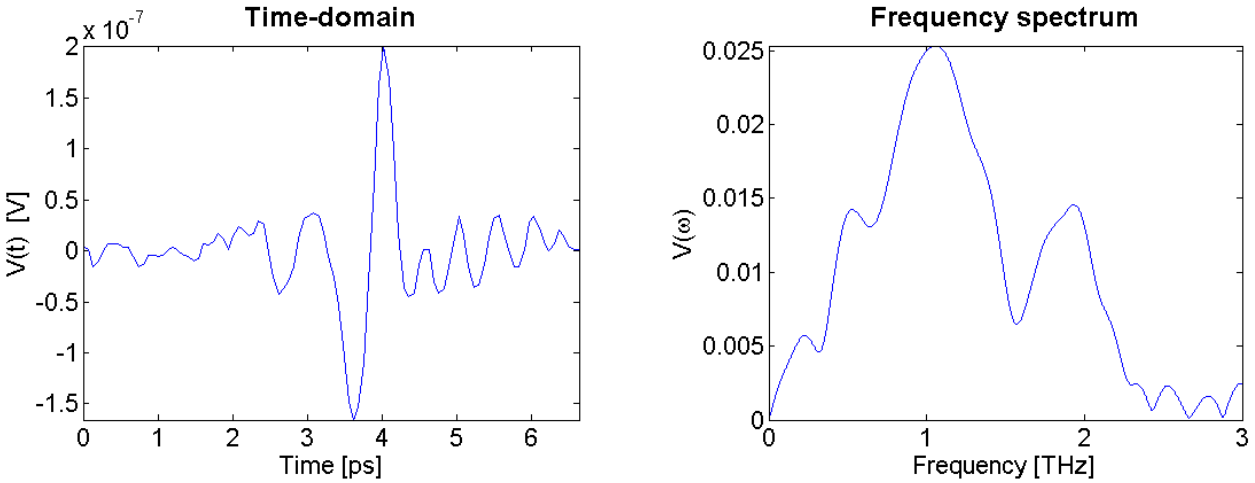


(a) Time-domain.

(b) Frequency-domain.

Figure 4.1: Results obtained from THz-TDS measurements with the new setup.

| Pump power | Probe power | Ref. freq | TC | Sensitivity | Step length | Scan length |
|---|---|---|---|---|---|---|
| 32 mW | $\sim 1$ $\mu$W | 125 Hz | 3 | 50 $\mu$V | 0.01 mm | 1.5 mm |

Table 4.1: Measurement settings for figure 4.1. Ref. freq and TC are abbreviations for reference frequency and time-constant used for the lock-in amplifier.

Figure 4.1 shows a THz-TDS measurement with no sample present. The results of this new setup was not better to begin with, if compared to the results from figure 3.13, but there were many improvements that could be made for this setup. The THz radiation in the setup used in figure 3.12 was to some degree focused, while the new setup was unfocused.

This setup was easier to work with since the beam stayed unfocused and the diameter of the two beams was the same through the whole system. The 800 nm light was also more efficiently removed for the pump beam. Once the infrared light had gone through the ZnTe generation crystal, most of it was removed by the transmittance through new ITO window and blocked directly after. The remaining 800 nm light was reflected by the thin silicon sample. By the time the THz beam arrived at the samples under investigation, no 800 nm light was present.

### 4.1.2 ZnTe crystal thickness and azimuthal angle

As mentioned under section 3.3.1, experimentalists tend to use thin generation crystals to avoid phase-matching issues. Therefore, the 2 mm ZnTe generation crystal was swapped with the 1 mm ZnTe detection crystal to see how this would affect the system. As a result of substituting the detection crystal of 1 mm thickness with a 2 mm crystal, the sensitivity of the system would increase since the interaction length in the crystal was longer. It would also increase the effects of phase mismatch and absorption, which would reduce the effective bandwidth of the electro-optic detection process. The results of changing the thickness of the crystals can be seen in figure 4.2.

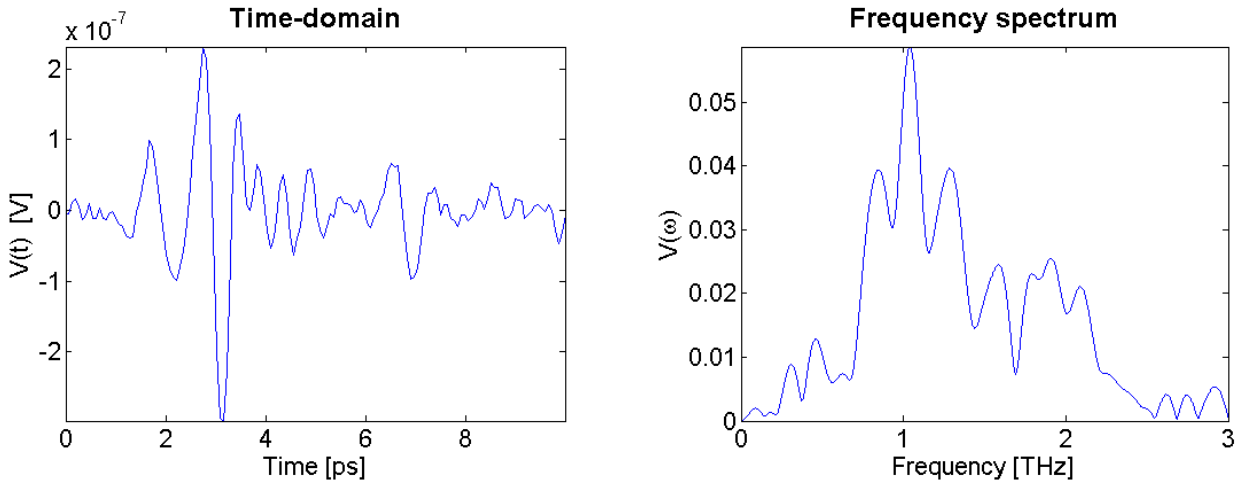


(a) Time-domain.

(b) Frequency-domain.

Figure 4.2: Results obtained from THz-TDS measurements after changing the thickness of the ZnTe generation crystal from 2 mm to 1 mm.

| Pump power | Probe power | Ref. freq | TC | Sensitivity | Step length | Scan length |
|---|---|---|---|---|---|---|
| 30 mW | $\sim 1$ $\mu$W | 125 Hz | 1 | 50 $\mu$V | 0.01 mm | 1.5 mm |

Table 4.2: Measurement settings for figure 4.2.

By comparing the frequency spectrum in figure 4.2b to figure 4.1b, one can see that the shape of the THz pulse has been altered. The system seemed to be more sensitive to perturbations and absorption, while the effective bandwidth might be slightly reduced. It is hard to tell as the amplitude had increased, for certain frequencies more than others. According to the literature [32] and equation 3.16, the amplitude of the emitted terahertz electric field should be reduced as the thickness of the generation crystal is decreased. The increased amplitude seen in figure 4.2b could to a certain degree be a result of a more sensitive system, but the most likely contributor was a more appropriate azimuthal angle for the crystals. As found in the literature [41], the azimuthal angle of the crystals were of great importance. An experiment was performed to find the optimum angles for the generation and the detection crystal.

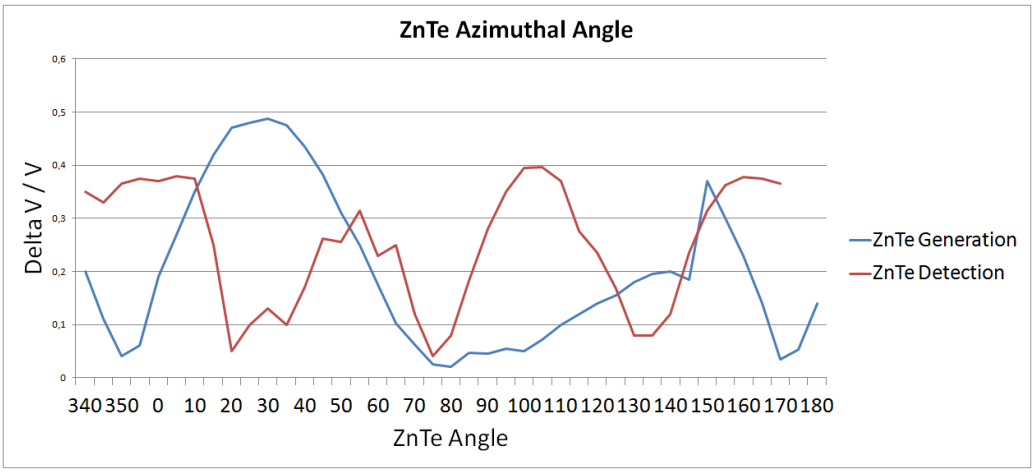


Figure 4.3: The figure displays the optimum angles for the ZnTe crystals used for generation and detection of THz.

Note that the angles of the crystals were for the crystals used in this work and not in general. That means that 0° is not necessarily 0° for others, it depends on how the crystals are inserted into their mounts. Finding the ideal angles were done by keeping one of the crystals at a constant angle, then rotating the other crystal with an interval of 5°. The measured signal would then increase or decrease as the angles varied, searching for the one with the strongest emitted terahertz electric-field. According to reference [41], the crystals are symmetric and were therefore only rotated 180°. The optimum angle for the generation crystal was found to be 30°, and 125° for the detection crystal.

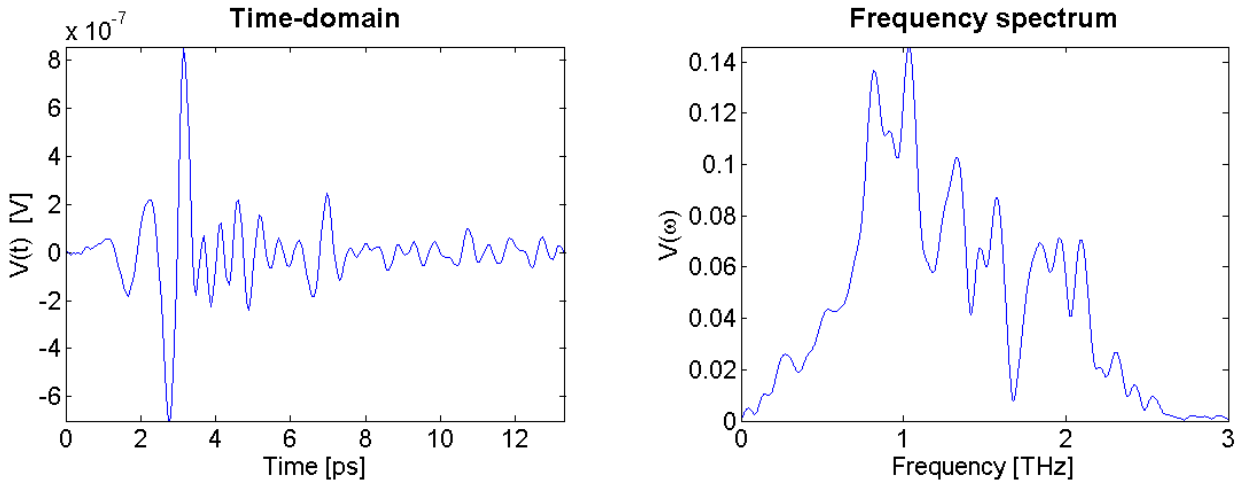


(a) Time-domain.

(b) Frequency-domain.

Figure 4.4: Results obtained from THz-TDS measurements after finding the optimum angles for the ZnTe crystals.

| Pump power | Probe power | Ref. freq | TC | Sensitivity | Step length | Scan length |
|---|---|---|---|---|---|---|
| 15 mW | $\sim 1$ $\mu$W | 125 Hz | 3 | 50 $\mu$V | 0.01 mm | 2 mm |

Table 4.3: Measurement settings for figure 4.4.

The results of changing the angles for the generation and the detection crystal can be seen in figure 4.4. One can clearly see the improvements of finding the optimum angle for the crystals in both the time-domain and frequency-domain as the signal was smoother and stronger. A pyroelectric detector was used to calculate the conversion efficiency of the system used in this thesis. The conversion efficiency for our system was $\eta = 1.34 \cdot 10^{-5}$, which is consistent with the literature that are typically in the range of $10^{-5} - 10^{-9}$ [10] [4].

### 4.1.3 Tube

As there were several experiments simultaneously in the laboratory, high panels were used to separate the experiments from each other. This was done to prevent reflections and stray light to interfere with the other experiments, in addition to be a safety measure. As a consequence, reflections from the chopper and other components was then reflected again by the panels; guiding the light towards the electro-optic detector. This additional light distorted the signal and buried it in noise. To prevent the unwanted light to go into the electro-optic detector, a small tube was made. The tube was inserted between the detector and the ZnTe detection crystal to make sure only the intended laser beam entered the detector.

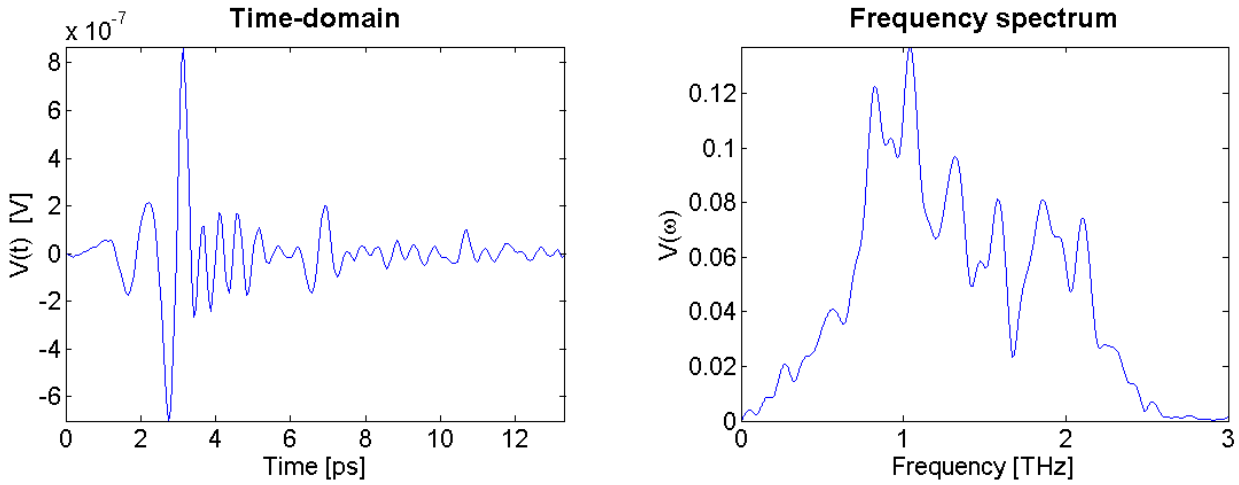


(a) Time-domain.

(b) Frequency-domain.

Figure 4.5: Results obtained from THz-TDS measurements with a tube in front of the electro-optic detector to prevent unwanted stray light and reflections to enter the detector.

| Pump power | Probe power | Ref. freq | TC | Sensitivity | Step length | Scan length |
|---|---|---|---|---|---|---|
| 15 mW | $\sim 1$ $\mu$W | 125 Hz | 3 | 50 $\mu$V | 0.01 mm | 2 mm |

Table 4.4: Measurement settings for figure 4.5.

The results in figure 4.5 are roughly the same as prior to the panels. There was less water absorption in this measurement than for the previous one, which can be seen for the typical frequencies for absorption of water at 1.2, 1.4, 1.7 and 2.1 THz. This had nothing to do with the tube that was introduced, it was due to a change in the relative humidity of the environment in the laboratory. By the fact that there was negligible difference between the signal in figure 4.4 and figure 4.5, one can state that the tube was a valuable addition to the setup as it prevented stray light and reflections to enter the electro-optic detector.

### 4.1.4 Chopper frequency 500 Hz

As mentioned in section 3.2, why people use 125 Hz for the chopper frequency was unclear so we increased the chopper frequency to 500 Hz to see how this would affect the results. By increasing the chopper frequency from 125 Hz to 500 Hz means that there were 4 times as many pulses for each measurement. With 125 Hz, every eight pulse was measured since the repetition rate for the laser was 1 ms. When the chopper frequency was 500 Hz, every second pulse was measured. This should increase the accuracy of the measurements since we had more points for each time interval and it also allowed for shorter data acquisition time. What shorter data acquisition time means in practice is that the time-constant for the lock-in amplifier can be reduced and still keep roughly the same signal-to-noise ratio (SNR).

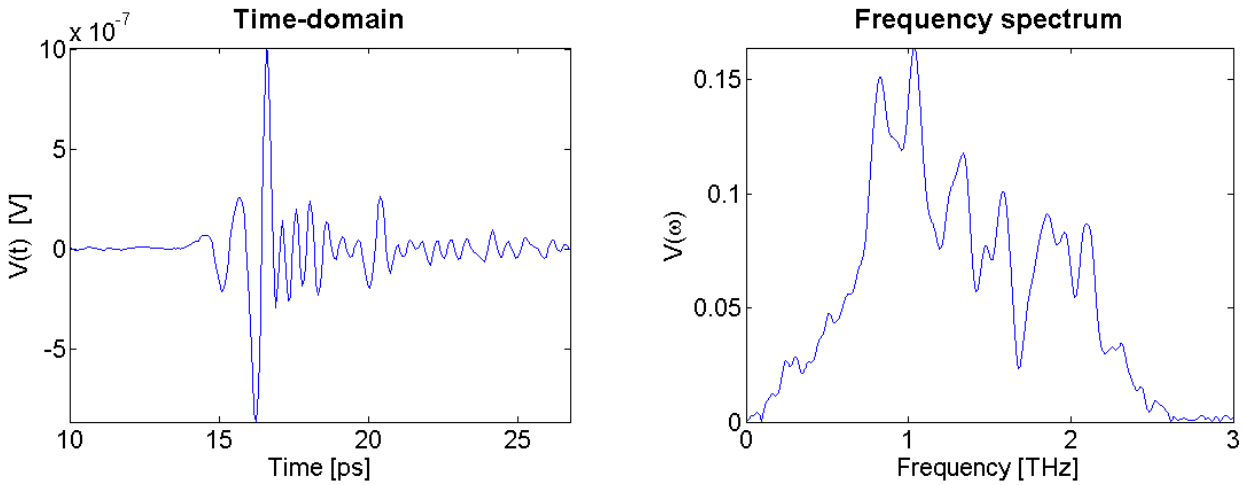


(a) Time-domain.

(b) Frequency-domain.

Figure 4.6: Results obtained from THz-TDS measurements after increasing the chopper frequency to 500 Hz.

| Pump power | Probe power | Ref. freq | TC | Sensitivity | Step length | Scan length |
|---|---|---|---|---|---|---|
| 60 mW | $\sim 1$ $\mu$W | 500 Hz | 3 | 50 $\mu$V | 0.01 mm | 4 mm |

Table 4.5: Measurement settings for figure 4.6.

One can see that amplitude increased slightly in both the time-domain and the frequency-domain, which could be caused by the increased accuracy of having more pulses to measure for each time-interval or by the fact that the average pump power increased as more pulses were let through. The average pump power was 15 mW, but as the chopper frequency was increased by a factor of 4; the average pump power was 60 mW. Regarding the data acquisition time and signal-to-noise ratio, experiments with the two different chopper frequencies were performed with different time-constants for the lock-in amplifier. We concluded these experiments with a relationship between the chopper frequency and time-constant for the lock-in amplifier in context with the signal-to-noise ratio. A chopper frequency of 500 Hz and time-constant of 3 seconds would roughly correspond to a chopper frequency of 125 Hz with a time-constant of 10 seconds to achieve the same SNR. The same for 500 Hz with 1 second time-constant to 125 Hz with time-constant of 3 seconds.

### 4.1.5 Pump power

To examine what pump power would result in the strongest electric field for the THz wave, various pump powers were tested by rotating the neutral density filter while the probe power was kept constant. It was kept constant to be able to compare the results with only one variable; the pump power. Experiments were performed on pump powers of 1 mW, 5 mW, 10 mW, 15 mW, 30 mW, 50 mW, 100 mW and 150 mW. The best result of these measurements were obtained with a pump power of 150 mW, which can be seen in figure 4.7. An increase of the pump power would result in a stronger electric field for the THz wave and a larger magnitude for the frequency spectrum, which was consistent with the literature [33] [5]. Other effects that arose by having stronger intensities was a reduction of the effective bandwidth and a shift of the centre frequency. For low intensities the spectrum had a broad effective bandwidth and was centred at $\sim 2.3$ THz. As the intensity increased, the effective bandwidth was reduced and the centre shifted progressively towards 1 THz [33].

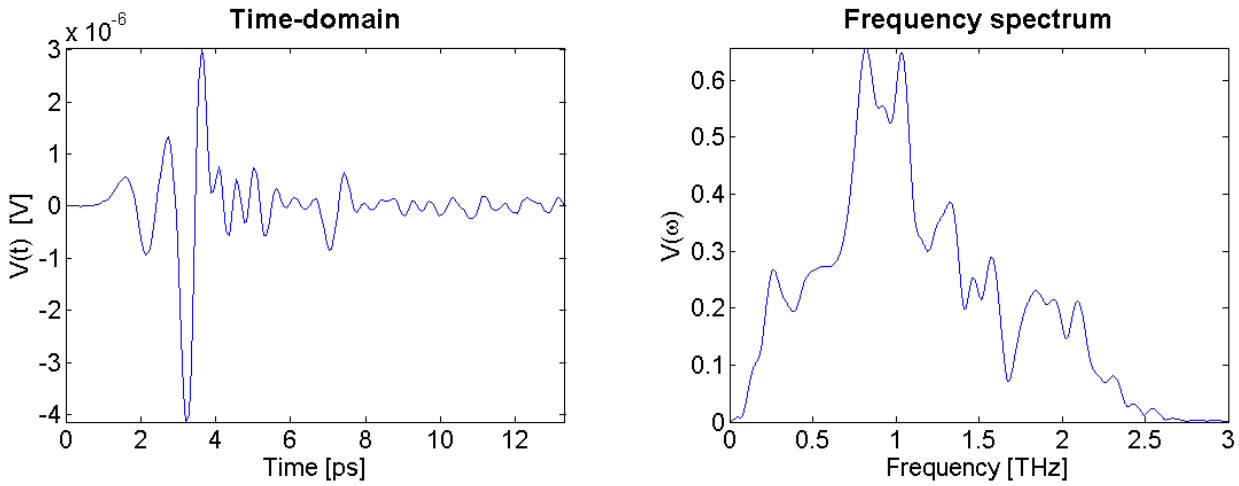


(a) Time-domain.

(b) Frequency-domain.

Figure 4.7: Results obtained from THz-TDS measurements after increasing the pump power to 150 mW.

| Pump power | Probe power | Ref. freq | TC | Sensitivity | Step length | Scan length |
|---|---|---|---|---|---|---|
| 300 mW | $\sim 1$ $\mu$W | 500 Hz | 10 | 50 $\mu$V | 0.01 mm | 2 mm |

Table 4.6: Measurement settings for figure 4.7.

By comparing figure 4.7b to figure 4.6b, increasing the pump power to 150 mW had a significant impact for the magnitude of the time-domain and the frequency spectrum. The results in figure 4.7 were obtained with a pump power of 150 mW, probe power of 1 $\mu$W, chopper frequency of 500 Hz and a time-constant of 10 seconds for the lock-in amplifier. The reason for increasing the time-constant for the lock-in amplifier from 3 seconds, used for the previous results, to 10 seconds is a consequence of higher pump power. The noise was enhanced as the pump power increased, therefore a longer time-constant was needed.

### 4.1.6 Photodetector for 1 kHz reference frequency

As mentioned under section 3.2, why no one uses the laser pulse itself as a reference signal was unclear. It results in shorter data acquisition times and no chopper is needed. Increasing the chopper frequency from 125 Hz to 500 Hz was a success; therefore it would be interesting to see how a reference frequency of 1 kHz would affect the results. A photodetector (model Newport 818-BB-21) replaced the chopper, where the reflection from the thin silicon sample used for blocking the 800 nm light was guided into the photodetector to set the reference signal. The reference frequency for the lock-in amplifier, which previously was the chopper frequency, was then triggered by the laser pulses itself at 1 kHz repetition rate. The results of changing the chopper with a photodetector can be seen in figure 4.8.

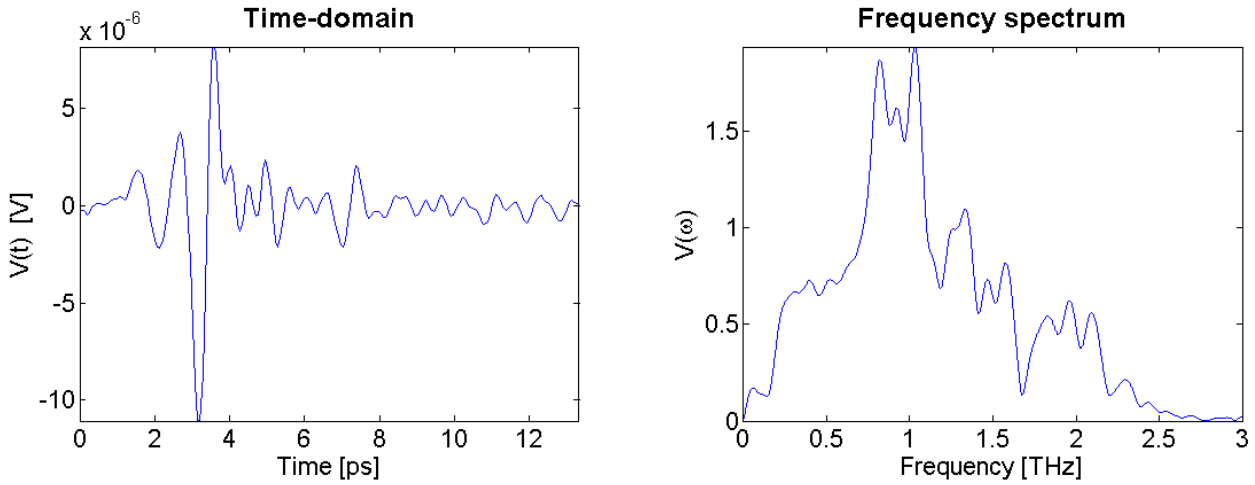


(a) Time-domain.

(b) Frequency-domain.

Figure 4.8: Results obtained from THz-TDS measurements with a photodetector to set the reference signal for the lock-in amplifier to 1 kHz. The pump power was increased to 300 mW.

| Pump power | Probe power | Ref. freq | TC | Sensitivity | Step length | Scan length |
|---|---|---|---|---|---|---|
| 300 mW | $\sim 1\ \mu$W | 1 kHz | 3 | 50 $\mu$V | 0.01 mm | 2 mm |

Table 4.7: Measurement settings for figure 4.8.

By substituting the chopper with a frequency of 500 Hz for a photodetector that triggered on the laser pulses itself, the setup had a reference frequency of 1 kHz and a data acquisition for every pulse. As an effect of this, the average pump power was doubled from 150 mW to 300 mW. As expected from the previous results, the increase in pump power produced more THz and was by far the best result obtained by these improvements. A pump power of 300 mW for the laser used in this work corresponded to an intensity of $10\frac{GW}{cm^2}$, which was 10% of the damage threshold of ZnTe. As mentioned in section 4.1.5 and 4.1.4; the noise level rose as the pump power was increased, but was to some degree compensated for by increasing the reference frequency and adjusting the time-constant. The results in figure 4.8 was obtained with a time-constant of 3 seconds. The time-constant could be increased to 10 seconds to improve the signal-to-noise ratio, but a time-constant of 3 seconds was found to be sufficient for a 1 kHz reference signal. Introducing the photodetector that triggered on the laser pulses had a favourable outcome and was used for further experiments. The only drawback we found by using the photodetector was the stability of the laser, which could at times slightly vary.

### 4.1.7 Nitrogen

THz waves are extremely sensitive to water absorption, as mentioned under section 3.4. The experiments performed in this thesis spans over 6 months and the relative humidity in the laboratory during this period of time varied between 15%-40%. Figure 4.9a shows the water absorption at different humidities, where the blue and green dotted lines represent the absorption relevant for this thesis. The absorption coefficient $\alpha$ for ZnTe at different room temperatures can be seen in figure 4.9b, where the solid line for 295 K was relevant for these experiments.

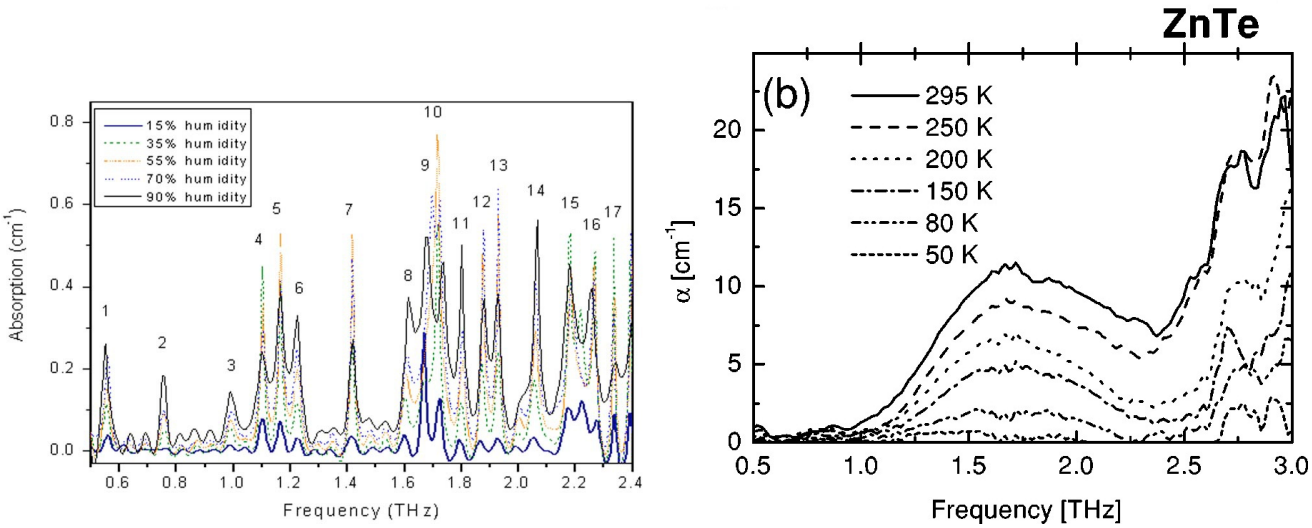


(a) Water absorption profiles at different humidities at room temperature for 0.2-2.4 THz.

(b) Absorption coefficient of ZnTe for different room temperatures for 0.2-3 THz.

Figure 4.9: Frequency spectra of the water absorption and the absorption coefficient of ZnTe [38] [27].

It was clear from figure 4.9a that the relative humidity had to be taken into consideration. By comparing the peaks for the water absorption to the frequency spectrum of the experiments, one can see how the water absorption affected the results. One can also see from figure 4.9b that the absorption coefficient of ZnTe contributes to the significant peak at $\sim 1.7$ THz for the frequency spectrum of our experiments. Since we had no control over the relative humidity of the environment and wanted more accurate measurements of our samples, a home-made airtight plastic box was built to be filled with nitrogen ($N_2$). The plastic box was placed over the area of the THz beam path, i.e. it covered the area from the ZnTe generation crystal to the ZnTe detection crystal. The pump and probe beam came into the box through N-BK7 laser windows, suitable for transmitting 800 nm light with a transmission of 99%, and exited the box through the same kind of laser window after the detection crystal. Everything involved with the THz radiation would then take place inside the plastic box with a nitrogen environment, reducing the water absorption of THz radiation. To effectively change the samples that were going to be measured, the area exposed to air when changing the samples had to be minimize. A small container of Plexiglas with a lid was therefore made to contain the samples and inserted into the plastic box, hanging from the top of the box. The samples could then be changed by opening the lid, exposing only the area inside the small container to air. The THz beam path would then travel through the container and the samples. To minimize the loss of THz, experiments were performed on Plexiglas, Saran wrap, paper, plastic and polytetrafluoroethylene to find a suitable material for THz transmission to act as windows for this container. Of these, Saran wrap was found to be the best material of choice for transmission of THz. Measurements were

performed before and after the plastic box and the container was filled with nitrogen. The two results are compared in figure 4.10.

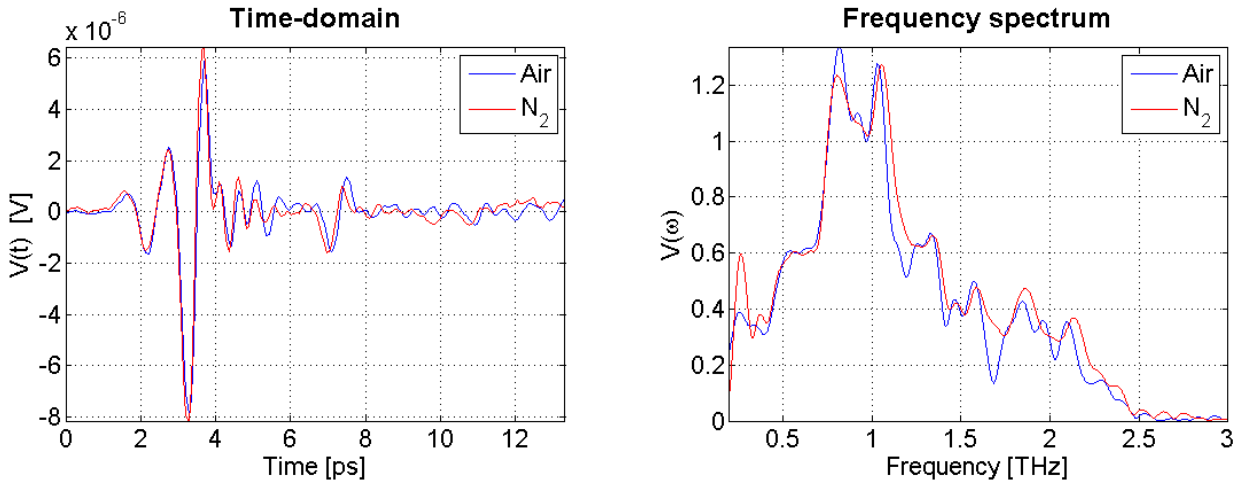


(a) Time-domain.

(b) Frequency-domain.

Figure 4.10: Results obtained from THz-TDS measurements with nitrogen $N_2$ are compared to air. The red line represents the measurement with nitrogen and the blue line represents the one with air.

| Pump power | Probe power | Ref. freq | TC | Sensitivity | Step length | Scan length |
|---|---|---|---|---|---|---|
| 300 mW | $\sim 1$ $\mu$W | 1 kHz | 3 | 50 $\mu$V | 0.01 mm | 2 mm |

Table 4.8: Measurement settings for figure 4.10.

Inflate and fill the box with nitrogen to get rid of the water molecules in the air had little effect on the magnitude, but the signal seemed more polished. As can be seen from the frequency spectrum in figure 4.10b, the absorption of THz was much less for the typical frequencies for water absorption. Particularly for the frequency of $1,7$ THz one can see a significant alteration. Even though the frequency spectrum was improved, it still looked like there was some absorption left. This may be due to a combination of the phonon resonances and absorption of ZnTe, but also an indication of that the plastic box was not completely airtight and fully filled with nitrogen. We did not have an effective method of monitoring the relative humidity inside the box as it was filled with nitrogen, so a detailed analysis could not be performed to determine what caused the remaining absorption. One should also keep in mind that the frequency spectra obtained for optical rectification through ZnTe are not as smooth as for photoconductive antennas.

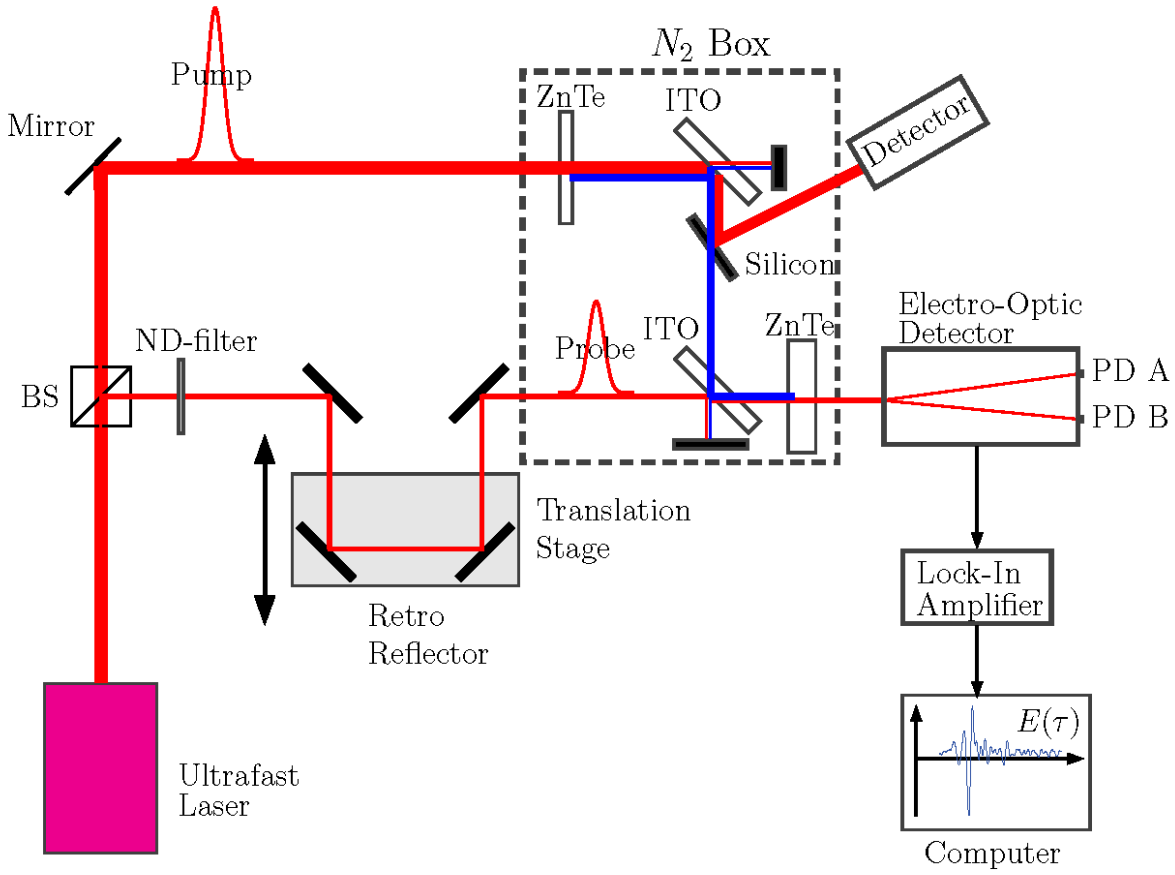


Figure 4.11: A schematic of the final setup for the THz-TDS system.

Figure 4.11 is a schematic of the final setup for the THz-TDS system. The red lines represent the 800 nm light and the blue line represents the THz radiation. The pump power was 300 mW and the probe power was $\sim 1$ $\mu$W. The variable time-delay of the THz pulse with respect to the probe pulse was given by $\tau$. The stippled lines represent the box used for creating a nitrogen environment. PD A and PD B are the two balanced photodiodes of the electro-optic detector. The detected signal was read by a lock-in amplifier, and the data was extracted to a personal computer.

### 4.1.8 Electric field strength of the THz radiation

The electric field strength of the THz radiation, $E_{THz}$, was found by using the calculations from section 3.5.2. $\Delta V$ and $V_{max}$ in equation 3.48 were found from the THz-TDS measurements as shown in figure 4.12.

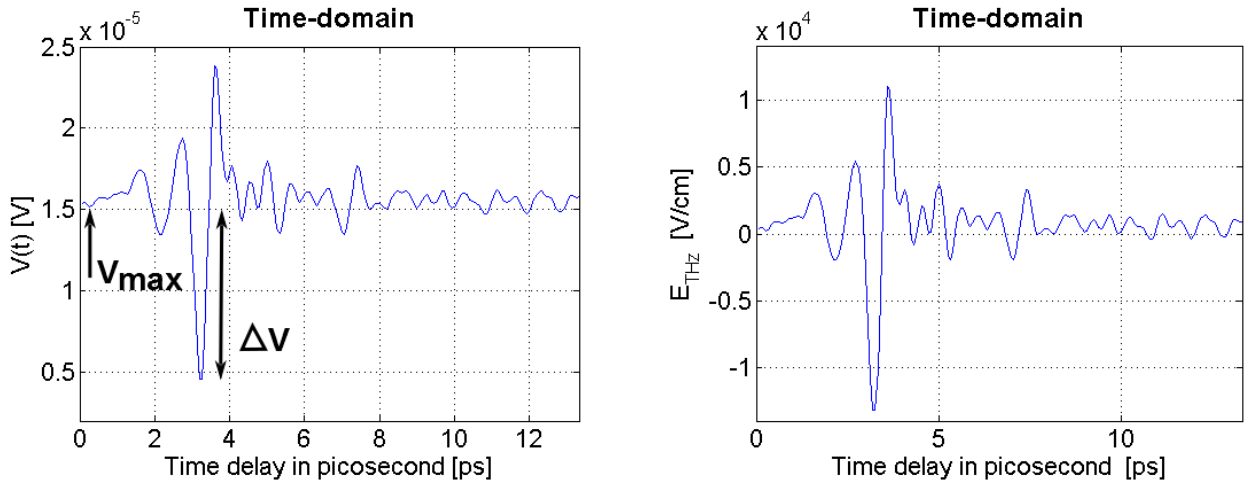


(a) How to find $\Delta V$ and $V_{max}$ from the signal.

(b) Corresponding electric field, $E_{THz}$.

Figure 4.12: $\Delta V$ and $V_{max}$ are found from the detected signal measured in volt in figure (a). The corresponding electric field strength $E_{THz}$ can be seen in figure (b).

| Pump power | Probe power | Ref. freq | TC | Sensitivity | Step length | Scan length |
|---|---|---|---|---|---|---|
| 300 mW | $\sim 1$ $\mu$W | 1 kHz | 3 | 50 $\mu$V | 0.01 mm | 2 mm |

Table 4.9: Measurement settings for figure 4.12.

$\Delta V$ was found by taking the maximum outcome of the detected signal, which occurred when $E_{THz}$ was applied, and subtracting it with the value in the absence of $E_{THz}$. The value in the absence of $E_{THz}$ can be seen in figure 4.12a as the value prior to the arrival of the THz pulse, referred to as $V_{max}$. The maximum outcome can either be positive or negative in relation to $V_{max}$, depending on the rotation of the quarter wave-plate in the electro-optic detector. When the power supply for the detector was disconnected and then re-connected, the quarter wave-plate might rotate to find the next time the two photodiodes in the detector were balanced. It was balanced two times during a round-trip, with a phase shift of 180° between each other. This would result in a change of the sign of the electric field, meaning that the maximum outcome could have a higher value than $V_{max}$ before disconnecting the power supply and then have a lower value when it was reconnected again because the quarter wave-plate might rotate 180°. Therefore, the sign of the detected electric field may be looked upon as arbitrary. The measured electric field did not change shape or value, it was just the sign of the electric field that might change and thereby flip the detected signal.

The maximum $\frac{\Delta V}{V_{max}}$ obtained in this thesis was $\sim 0,7$, which corresponded to an electric field strength of $E_{THz} = 13,2\frac{kV}{cm}$ according to eq. 3.48. The electric field strength for the first THz-TDS setup was $0,45\frac{kV}{cm}$, and by improving this setup we were able to increase it by $10^2$ orders of magnitude. The THz beam used in this setup was unfocused. By focusing the beam it should be possible to acquire a stronger electric field. By using lenses which are suitable for THz to focus the beam, the electric field strength could be increased by at least an order of $10^2$. Focusing the beam would result in an electric field strength in the order of $\frac{MV}{cm}$.

### 4.1.9 Signal-to-noise ratio and dynamic range of the experiments

The best signal-to-noise ratio (SNR) and dynamic range (DR) obtained during these experiments were $SNR = 43$ and $DR = 1500$ by using the method recommended from reference [22], which is discussed under section 3.5.3. The SNR and DR obtained in reference [22] were 120 and 9900, but were acquired by the use of photoconductive antennas which have better SNR and DR than what can be obtained by optical rectification. The SNR and DR in this thesis were lower than the results from the experiments in this article, but that was expected as the method of optical rectification and electro-optic detection were used. The results we obtained were still roughly in the same order of magnitude as the ones from reference [22]. The other method described in this article was also tested on our results, but it was more inaccurate and has some flaws. As given by equation 3.52, it uses an average for the entire measurement. When using this method on the first results, seen in figure 3.13a, it gives a good SNR because the measurement begins far from the arrival of the THz pulse. Using the recommended method with the same data, the SNR would be much less. The other measurements usually started closer to the THz pulse and would not give a long flat signal to begin with as the first measurement did. This means that the other method of calculating the SNR and DR depends more on how long the measurements are done prior to the arrival of the THz pulse, instead of the actual signal. Many published articles only announce the best SNR and DR they've achieved, and not the method of how they were obtained. As there were several ways to do this, and the results might vary for the same data, we found the recommended method from reference [22] the most reliable.

The sensitivity and time-constant for the lock-in amplifier also played a significant role for the SNR and DR, in addition to how they were calculated. Most of the results were obtained with a sensitivity of $50\mu V$, except the first one which had a sensitivity of $100\mu V$. Lower sensitivity for the lock-in amplifier would result in a more sensitive system, and noise was more easily detected. The time-constant for the lock-in amplifier used an averaging for each time-interval of the measurement, and was therefore able to filter out some of the noise. By increasing the time-constant one are able to get a more accurate value of the signal, and the SNR will improve.

### 4.1.10 A summary of the improvements

To improve the first THz-TDS setup that was made in this thesis, a new setup was built without paraboloidal mirrors. This new setup was easier to work with since it was unfocused and collinear through the system. It also had a more efficient way of getting rid of 800 nm light prior to the sample. The thickness of the generation and the detection crystal was changed to increase the conversion efficiency and sensitivity of the system. Experiments were performed to find the optimum azimuthal angle for the crystals. Modifications made to the experimental table in the laboratory resulted in stray light and unwanted reflections entering the electro-optic detector. A small tube between the detection crystal and the electro-optic detector was made to prevent this. Different chopper frequencies and a photodetector were tested to see how this would affect the signal-to-noise ratio and the time-constant needed for the lock-in amplifier. Measurements of various pump powers were performed to see how the generation of THz was related to the intensity. Last, a nitrogen environment was built to reduce the water absorption in air. A comparison of the results between the first THz-TDS setup and the setup after improvements were made, which can be seen in figure 4.13.

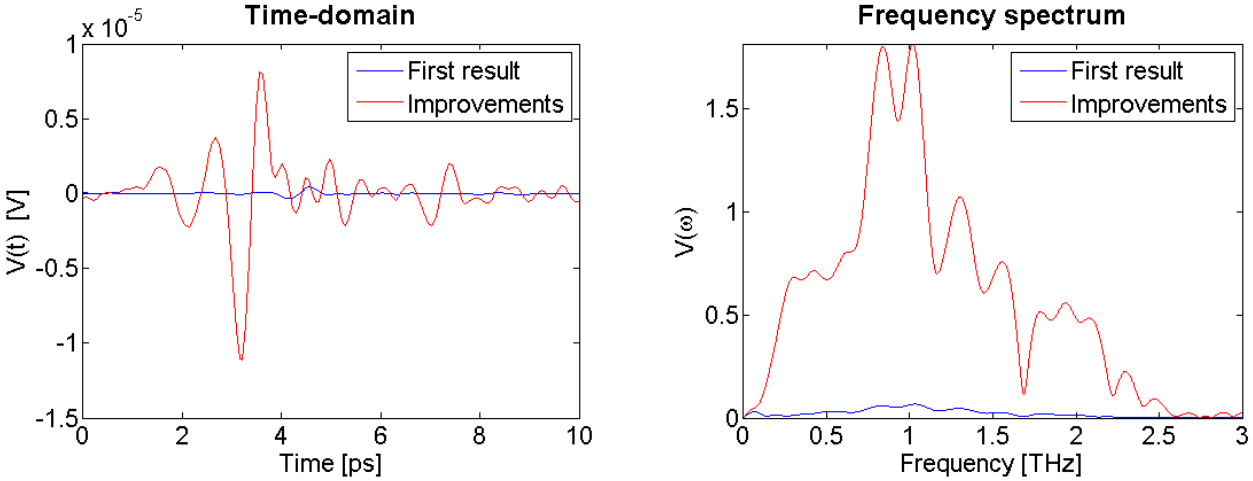


(a) Time-domain.

(b) Frequency-domain.

Figure 4.13: A comparison of the first setup and the setup after improvements used in this thesis. The blue line represents the first setup, and the red line represents the setup after improvements were made.

The THz-TDS measurements were significantly enhanced by the improvements that were made, which can be seen in figure 4.13. The magnitude was in the order of $10^2$ higher than the first obtained result. The most noteworthy contributors for optimizing the THz-TDS setup were the azimuthal angle of the ZnTe crystals and the pump power. Finding the optimum angle for the ZnTe crystals increased the conversion efficiency for generation of THz and the sensitivity of the system, which can be seen by comparing figure 4.4b to 4.2b. Increasing the pump power resulted in a stronger electric field for the THz radiation, but it also produced more noise. To obtain a smooth signal, a longer time-constant for the lock-in amplifier was necessary as the pump power was increased. Experiments on different chopper frequencies and eventually the use of a photodetector as a trigger for the reference frequency resulted in shorter data acquisition times and better signal-to-noise ratio. Increasing the reference frequency could to some degree compensate for the longer time-constants needed for higher pump powers, and the time-constant could then remain the same.

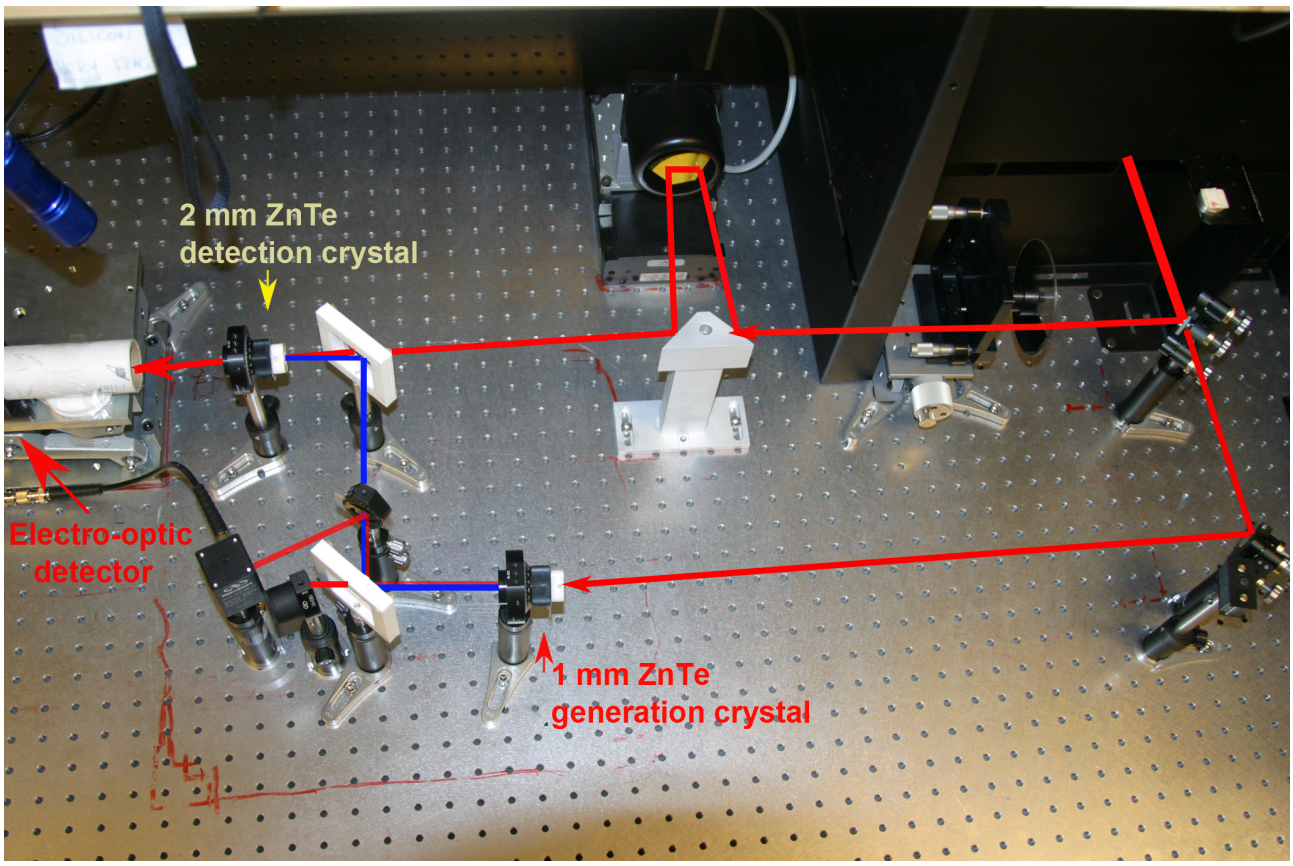


Figure 4.14: A picture of the final THz-TDS setup. The red lines are 800 nm light and the blue line is the THz radiation.

The THz-TDS setup can be seen in figure 4.14. It is depicted without the box containing nitrogen. The red lines represent the 800 nm light for the pump and probe beam, the blue line is the THz radiation generated in the first ZnTe crystal and detected in the second ZnTe crystal. The box was placed along the red lines marked on the table, covering the area from the generation crystal to the detection crystal. The electro-optic detector cannot be seen in this picture, but was placed immediately after the white tube on the left side.

## 4.2 Applications

As described under section 3.4, THz-TDS can be used to measure and analyse a wide range of materials. THz-TDS is excellent as a spectroscopic utility, with an immense diversity of applications and analytical purposes. One of the advantages of THz-TDS is that the setup can remain the same, indifferent to the mediums under investigation that may be utterly disparate. The sample simply has to be placed along the THz beam path before the THz wave and probe beam are combined, i.e. prior to the ITO window used for combining the two beams. This section will present the results obtained from measurements performed on a semiconductor and a wood sample.

### 4.2.1 Semiconductors

To perform a THz-TDS analysis on a semiconductor, two measurements were necessary. The first was a measurement without any sample, which would be used as a reference. The second was an equivalent measurement, but with the sample under investigation. The sample was placed along the THz beam path, i.e. between the thin silicon sample used for blocking the 800 nm light and the ITO window used for combining the THz and probe beam. The results from the two frequency spectra were then compared to perform the analysis. There were performed measurements on numerous types of semiconductors, where the one presented in this thesis was a wafer of silicon nitride ($Si_3N_4$). It is adequate to present the results for only one of these semiconductors, since the principle and analysis of the measurements are the same.

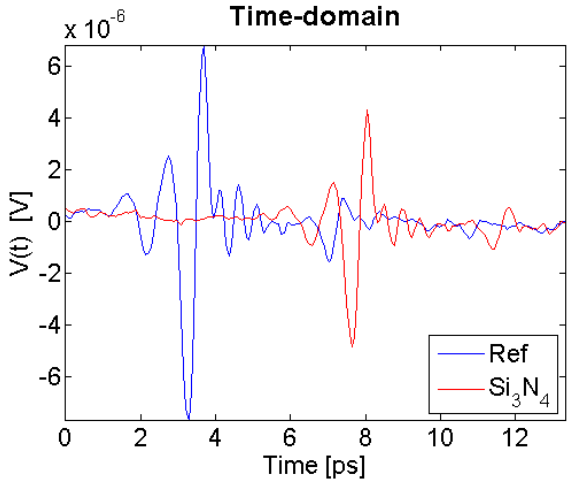


(a) Time-domain.

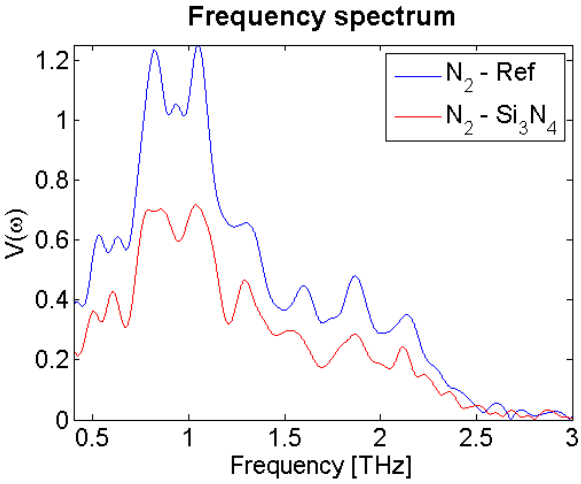


(b) Frequency-domain.

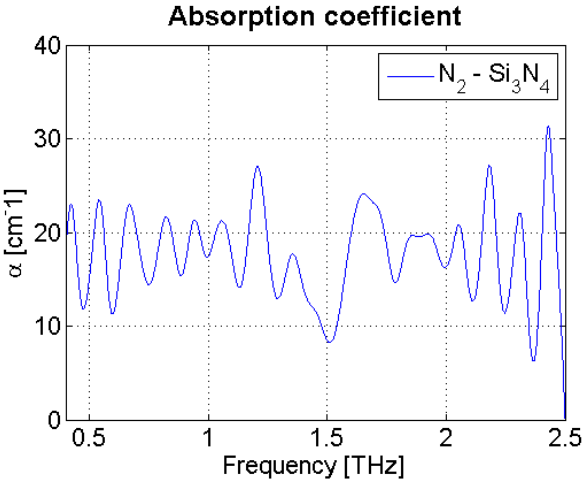


(c) Absorption coefficient.

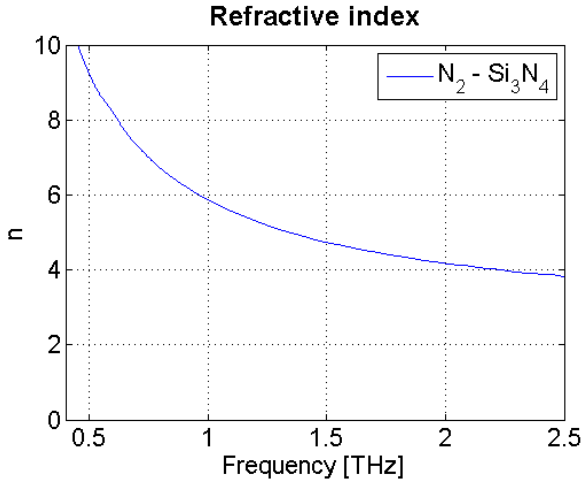


(d) Refractive index.

Figure 4.15: Results obtained from THz-TDS measurements of $Si_3N_4$ were compared to the reference signal. The measurements were performed in a nitrogen ($N_2$) environment. The blue line represents the reference scan, and the red line represents the $Si_3N_4$ semiconductor.

| Pump power | Probe power | Ref. freq | TC | Sensitivity | Step length | Scan length |
|---|---|---|---|---|---|---|
| 300 mW | $\sim 1$ $\mu$W | 1 kHz | 3 | 50 $\mu$V | 0.01 mm | 2 mm |

Table 4.10: Measurement settings for figure 4.15.

The results of the THz-TDS performed on $Si_3N_4$ are presented in figure 4.15. The measurements were done in a nitrogen ($N_2$) environment to prevent absorption by the water molecules in the air. The blue line is the reference scan without any sample, and the red line is the semiconductor of type silicon nitride ($Si_3N_4$). From figure 4.15a, it was obvious that the THz pulse had been delayed in time as it went through the sample. The delay in time depended on the type of material and the thickness of the sample. The amplitude for the sample was smaller than for the reference because the beam got attenuated as it travelled through a material. Even though the measurement for the sample had a lesser amplitude, it had a similar shape as the reference for both the time-domain and the frequency-domain. This was not always the case, the shape of the pulse depended on the type of material that was being investigated. The derivations from the literature [14], found under section 3.5.1, were used to analyse the absorption coefficient and the refractive index of the material. Figure 4.15c and 4.15d presents the analytical results for the absorption coefficient and the refractive index of $Si_3N_4$, which varies with the frequency. The information provided by THz-TDS can also be used to find the conductivity of the material [30] [39].

### 4.2.2 Wood

Experiments were also performed on three different kinds of wood; oak, pine and spruce. The properties of wood are of great interest for the industry. As mentioned under section 3.4, THz waves are extremely sensitive to water absorption. For this reason, THz-TDS can be used as a method to measure the water content of wood samples. Being able to measure the humidity of wood is important for the industry, as it can identify what kind of drying processes are the most efficient. An analysis of the humidity of the wood samples will not be performed in this thesis, but the principle of how to obtain the necessary information is similar as for semiconductors and other materials. Similar to the semiconductors results, it is adequate to present only one of the wood samples.

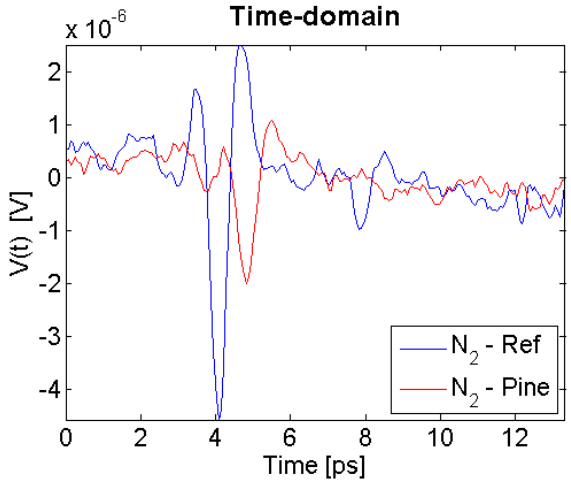


(a) Time-domain.

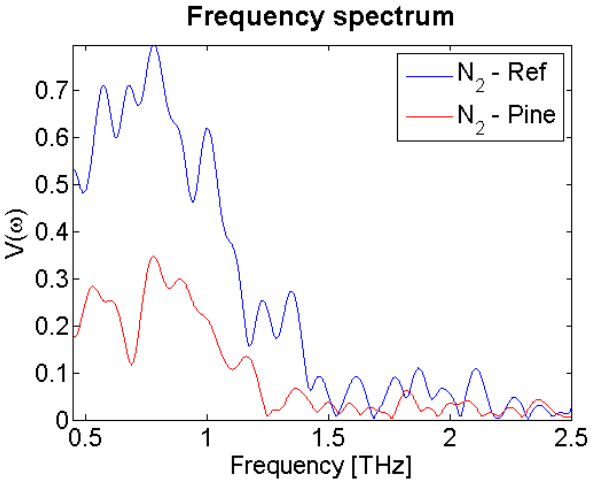


(b) Frequency-domain.

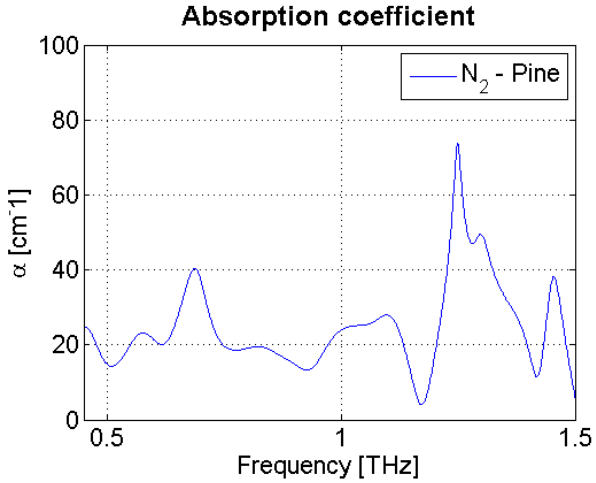


(c) Absorption coefficient.

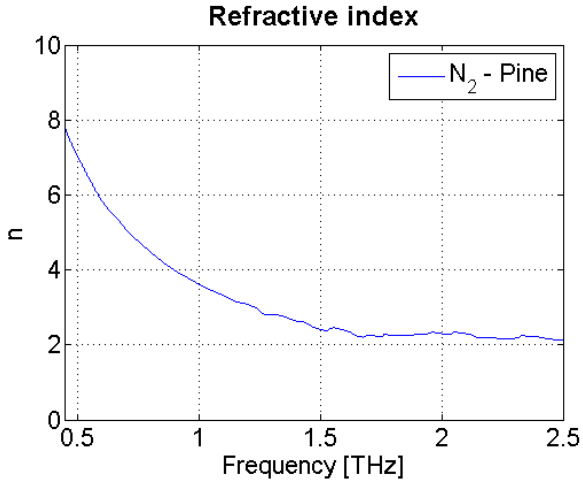


(d) Refractive index.

Figure 4.16: Results obtained from THz-TDS measurements of pine are compared to the reference scan. The measurements are performed in a nitrogen ($N_2$) environment. The blue line represents the reference signal and the red line is the sample of pine.

| Pump power | Probe power | Ref. freq | TC | Sensitivity | Step length | Scan length |
|---|---|---|---|---|---|---|
| 300 mW | $\sim 1$ $\mu$W | 1 kHz | 3 | 50 $\mu$V | 0.01 mm | 2 mm |

Table 4.11: Measurement settings for figure 4.16.

Figure 4.16 presents the results obtained by THz-TDS performed on pine in a nitrogen ($N_2$) environment. The results are presented slightly different than that of the semiconductor. Wood had a different signature than the semiconductors, so the shape of the pulse was altered. The results in figure 4.16 were obtained by using a 0.92 mm thin sample of pine as a reference instead of dry air. The sample under investigation had a thickness of 1.81 mm, and was compared to the thin reference sample. By using the same material as a reference and as a sample, the difference between them would then be the thickness and the humidity. The thickness can easily be measured, but the humidity is a bit more complicated. To measure the humidity of the sample, the humidity of the reference sample has to be known.

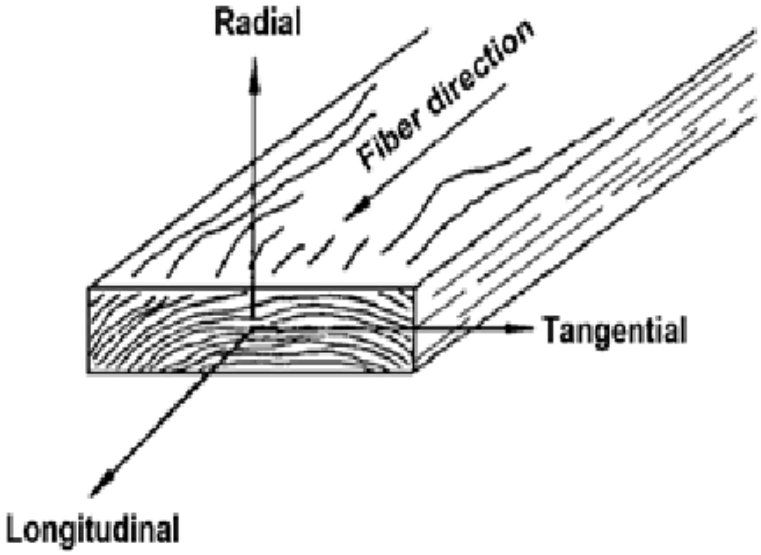


Figure 4.17: Three principal axis of wood with respect to the grain direction and growth rings [19].

Note that the orientation of the sample with respect to the fibre direction of the wood, as seen in figure 4.17, are of great importance for the results. There are three principal axes with respect to the grain direction and growth rings; radial, longitudinal and tangential. The measurements in this thesis were done with respect to the radial axis of the woodwork [19].

# Chapter 5

# Future work

For future work with THz-TDS with the methods of optical rectification and free-space electro-optic sampling, further improvements can be made.

To enhance the generated electric field strength $E_{THz}$, there are two main modifications that can be made. Increasing the pump power even more, but the damage threshold of the crystal has to be kept in mind not to destroy it. The intensity of $E_{THz}$ can also be greatly enhanced by focusing using lenses suitable for THz. Focusing would increase the electric field strength of at least $10^2$ orders of magnitude. Depending on the desired abilities for the system; with a stronger electric field, the detection crystal could be changed to a thinner crystal to increase the effective detectable bandwidth and still have sizeable amplitude.

Another important aspect of the system, once the THz radiation has been generated, is to minimize the loss of transmission through components. ITO windows have a $80\% - 90\%$ reflectivity of THz radiation, but was an efficient way of getting rid of 800 nm light. Saran wrap for the sample container has a decent transmission of THz radiation, but there may be other more promising materials for this purpose. The component with the lowest transmission efficiency in the setup used in this thesis was the thin silicon sample used for getting rid of the remaining 800 nm light, where 45% of the THz transmission was lost.

As mentioned under section 4.1.7, the plastic box filled with nitrogen was suspected not to be completely airtight as it was a provisional solution. A new airtight container should be made to prevent leakage of nitrogen. Secondly, a wireless humidity monitor would be useful to supervise the humidity of the nitrogen environment. The system could also be realigned to make a more compact system to minimize the length of the optical beam path to reduce the water absorption in air.

# Chapter 6

# Conclusion

Terahertz time-domain spectroscopy has proven itself as a utility with great potential in many active fields, such as medical diagnostics, security imaging and detection of explosives. The overall purpose of this thesis was to establish a THz-TDS system based on optical rectification and free-space electro-optic sampling (FSEOS) in zinc telluride (ZnTe) crystals, as well as exploring the possibilities to improve and optimize this setup. The most significant improvements to the THz-TDS system in this thesis are concluded to be the pump power used for the generation of THz and the azimuthal angle of the ZnTe crystals.

Increasing the pump power results in a stronger electric field for the THz radiation, as long as it does not exceed the damage threshold of the generation crystal. Finding the optimum azimuthal angle for the generation crystal was crucial to increase the conversion efficiency for THz emission, as to the detection crystal. Other noteworthy contributors were also found for improving the THz-TDS system. In this thesis, a photodetector to trigger on the laser pulses itself as a reference signal provided an adequate signal-to-noise ratio without the need for long time-constants for the lock-in amplifier. A dry nitrogen environment was formed to reduce the absorption of water molecules in air at certain frequencies. To prevent unwanted stray light and reflections into the electro-optic detector, a small tube was mounted in front of the detector to ensure that only the intended laser beam entered the detector and was found to be a useful addition to the setup. THz-TDS experiments were performed on semiconductors and wood. The obtained results were analysed to find the frequency spectra, the absorption coefficient and the refractive index of the materials. The spectroscopic information obtained by THz-TDS can also be used for finding the conductivity and mobility of the materials.

A THz-TDS system was built and improved through experimental work where the magnitude of the THz radiation was increased by an order of $10^2$ compared to the first setup in this thesis. The maximum detected electric field strength of THz radiation was $13.2\frac{\text{kV}}{\text{cm}}$. The THz waves in the setup used in this thesis were unfocused. By using lenses that are suitable for focusing THz radiation, such as paraboloidal gold mirrors, it should be possible to reach field strengths of several $\frac{\text{MV}}{\text{cm}}$. Publications are often given in arbitrary units so it is arduous to compare our results, but the ones that are found are often in the order of $0.5\frac{\text{kV}}{\text{cm}} - 1\frac{\text{kV}}{\text{cm}}$. Although, a peak electric field strength of $1\frac{\text{MV}}{\text{cm}}$ has been demonstrated in the literature using optical rectification and FSEOS. The conversion efficiency of the system was found to be $\eta = 1.34 \cdot 10^{-5}$.

There are no commonly agreed standard of calculating the signal-to-noise ratio (SNR) and dynamic range (DR) of a THz-TDS system, but there is a recommended practice in the literature

[22] of defining these quantities. The highest achieved SNR was 43 and DR of 1500 by the use of the recommended method from the literature. The SNR and DR of the experiments performed by others who used this method were 120 and 9900, but they used photoconductive antennas instead of optical rectification and FSEOS. Photoconductive antennas have better SNR and DR than what can be achieved by optical rectification and FSEOS, so it was expected that our results had a lower SNR.

There are still some improvements that can be made for future work on the setup presented in this thesis, such as focusing and finding components more suitable for transmitting THz radiation. Further, a new container should be made to ensure a completely sealed nitrogen environment with a humidity monitor inside to have control of all the parameters during the measurements.

# REFERENCES


[1] About lock-in amplifiers.

[2] What is a lock-in amplifier? Apr 2000.

[3] J.B. Baxter and G.W. Guglietta. Terahertz spectroscopy. May 2011.

[4] F. Blanchard, H.C. Bandulet, L. Razzari, G. Sharma, R. Morandotti, J.C. Kieffer, and T. Ozaki. High-power terahertz pulses at the advanced laser light source (alls) laboratory. 2007.

[5] F. Blanchard, L. Razzari, H.C. Bandulet, G. Sharma, R. Morandotti, J.C. Kieffer, T. Ozaki, M. Reid, H.F. Tiedje, H.K. Haugen, and F.A. Hegmann. Generation of 1.5 $\mu$ j single-cycle terahertz pulses by optical rectification from a large aperture znte crystal. 15(20), Oct 2007.

[6] Michael R. Boersma. An introduction to terahertz electromagnetic waves generation, detection properties and applications.

[7] Reshmi Chakkittakandy. Quasi-near field terahertz spectroscopy. Master's thesis, Indian Institute of Technology, Jan 2010.

[8] Newport Corporation. Solstice one box ultrafast amplifiers. http://www.newport.com/Solstice-One-Box-Ultrafast-Amplifiers/564081/1033/info.aspx, 2012. [Online; Accessed 23-June-2012].

[9] L. DeHua, Q. XiaoDong, and L. ShengGang. A theoretical analysis of optical-to-thz conversion efficiency via optical rectification. 51, Dec 2008.

[10] L. Dehua, Q. Xiaodong, Z. Wei, J. Tao, and L. Shenggang. Optical-to-thz conversion efficiency analysis and comparison of znte, dast, linbo3 crystals. 2009.

[11] G. Gallot and D. Grischkowsky. Electro-optic detection of terahertz radiation. 16, Aug 1999.

[12] G. Gallot, J. Zhang, R.W. McGowan, J. Tae-In, and D. Grischkowsky. Measurements of the thz absorption and dispersion of znte and their relevance to the electro-optic detection of thz radiation. 74, Jun 1999.

[13] Stefan Gorenflo. *A comprehensive study of macromolecules in composites using broadband terahertz spectroscopy.* PhD thesis, Albert Ludwigs University, Nov 2006.

[14] Hermann Harde. Time-domain spectroscopy of subps-thz-pulses. Apr 2009.

[15] S.M. Harre, R.L. Milot, J.M. Schleicher, and C.A. Schmuttenmaer. Influence of free-carrier absorption on terahertz generation from znte(110). *Applied Physics 107*, Feb 2010.

[16] Andrew D. Jameson. *Generating and using terahertz radiation to explore carrier dynamics of semiconductor and metal nanostructures*. PhD thesis, Oregon State University, Jan 2012.

[17] Franz X. Kaertner. Mode-locked laser theory. Oct 2006.

[18] G.Kh. Kitaeva. Terahertz generation by means of optical lasers. *Laser Phys.*, May 2008.

[19] David E. Kretschmann. *Wood handbook*. Department of agriculture, Madision, WI, 2010.

[20] C. Kubler, R. Huber, and A. Leitenstorfer. Ultrabroadband terahertz pulses: generation and field-resolved detection. Jun 2008.

[21] J.R. Morris and Y.R. Shen. Theory of far-infrared generation by optical mixing. 15, Mar 1977.

[22] M. Naftaly and R. Dudley. Methodologies for determining the dynamic ranges and signal-to-noise ratios of terahertz time-domain spectrometers. Apr 2009.

[23] M. Naftaly and R.A. Dudley. Calibration of terahertz spectrometers.

[24] A. Nahata, A.S. Weling, and T. Heinz. A wideband coherent terahertz spectroscopy system using optical rectification and electro-optic sampling. Aug 1996.

[25] Laboratory of Terahertz spectroscopy. http://lts.fzu.cz/en/intro.htm, 2012. [Online; Accessed 30-June-2012].

[26] Paul C.M. Planken. Measurement and calculation of the orientation dependence of terahertz pulse detection in znte. 18, Mar 2001.

[27] M. Schall, M. Walther, and P. Jepsen. Fundamental and second-order phonon processes in cdte and znte. Aug 2001.

[28] Y.R. Shen. *The Principles of Nonlinear Optics*. John Wiley and Sons, New York, 1984.

[29] S. Sirbu. *Induced excitations in some metal oxides*. PhD thesis, Rijksuniversiteit Groningen, 2008.

[30] J. Tae-In. *New applications of THz Time-domain spectroscopy*. PhD thesis, Oklahoma State University, May 1997.

[31] D. Turchinovich. *Study of Ultrafast Polarization and Carrier Dynamics in Semiconductor Nanostructures: a THz Spectroscopy Approach*. PhD thesis, Albert Ludwigs University, May 2004.

[32] N.C.J. van der Valk and P.C.M. Planken. Influence of pump wavelength and crystal length on the phase matching of optical rectification. 22, Aug 2005.

[33] S. Vidal, J. Degert, M. Tondusson, J. Oberle, and E. Freysz. Impact of dispersion, free carriers and two photon absorption on the generation of intense thz pulses in znte crystals. May 2011.

[34] X. Wang, Y. Cui, W. Sun, J. Ye, and Y. Zhang. Terahertz polarization real-time imaging based on balanced electro-optic detection. 27(11), Nov 2010.

[35] Andrew M. Weiner. *Ultrafast Optics*. Wiley, Hoboken, first edition, 2009.

[36] I. Wilke and S. Sengupta. Nonlinear optical techniques for terahertz pulse generation and detection - optical rectification and electrooptic sampling. Master's thesis, Rensselaer Plytechnic Intistute.

[37] Q. Wu, M. Litz, and X.C. Zhang. Broadband detection capability of znte electro-optic field detectors. Mar 1996.

[38] X. Xin, H. Altan, A. Saint, D. Matten, and R.R. Alfano. Terahertz absorption spectrum of para and ortho water vapours at different humidities at room temperature. Nov 2006.

[39] M. Yamashita, C. Otani, H. Okuzaki, and M. Shimizu. Nondestructive measurement of carrier mobility in conductive polymer pedot:pss using terahertz and infrared spectroscopy. In *General Assembly and Scientific Symposium, 2011 URSI*, pages 1 –4, aug. 2011.

[40] A. Yariv. *Optical Electronics in Modern Communications*. Oxford University Press, New York, 5th edition, 1997.

[41] Z.Y. Zhao, S. Hameau, M. Voos, and J. Tignon. Thz generation by optical rectification and competition with other nonlinear processes. May 2006.

# APPENDICES

# Appendix A

# Lock-in amplifier

## A.1 Lock-in amplifier

This appendix outlines the procedure of how to use the lock-in amplifier.

## A.2 Reset

Disconnect all cables from the lock-in. When turning on the lock-in amplifier the [Setup] button must be held down while the lock-in is starting up. This is to reset the instrument and delete previous data and setups from earlier measurements.

## A.3 External reference

It is important that the settings are assigned to take a reference signal as an input and not an internal signal generated by the lock-in. Hence, make sure the light "internal" under Source is OFF. Push the button so the "Pos edge" is ON. An external reference signal can now be measured. To check that the detector detects the desired signal and the chopper signal works properly, connect both of them to an oscilloscope to make sure the signals are correct.

## A.4 Set the reference signal

The next step is to set the reference signal. To do so, the detector must be connected to the lock-in through the A/I input.

*Reference frequency*: The chopper is connected to the "Ref In" input on the lock-in amplifier through the frequency generator. To verify that the chopper is connected correctly, the reference frequency can be shown on the lock-in by pushing the [Freq] button under the "Reference" panel. The correct chopper frequency should now be shown in the display to the right.

*Reference phase*: Since only the pump is passing through the chopper, the pump pulse must be used in order to set the reference phase. The probe is now blocked to only measure the pump.

The intensity of the pump is reduced and modified to prevent saturation in the detector. The detector is connected to the lock-in through the A/I input, that will show the pump signal as a function of X and Y, or R and $\theta$. The reference phase is set by following the steps below:

Press [Auto phase]. Automatically adjust the reference phase shift to eliminate any residual phase error.

Press [Phase] under "Reference" panel. This displays the reference phase shift in the reference display.

Press [+90]. This adds 90° to the reference phase shift. X and Y switch values so that X = Y and Y = -X.

Use the knob to adjust the phase shift until Y is zero and X is equal to the positive amplitude. Press [Auto Phase], this return Y to zero and X to the amplitude.

Press [Freq] to show the frequency of the reference in the reference display.

There should now be a 90° difference in the reference phase output when the pump is blocked and open.

The address for the lock-in amplifier should be set to 1 to match the MATLAB script for the computer. The address can also be changed in the script, as long as it corresponds to the one set for the lock-in amplifier.

The reference signal is now set and the pump beam is removed from the detector and replaced by the probe beam.

## A.5 Set important parameters

Some parameters need to be set to a suitable value to make a good measurement. *Sensitivity* and *Time-constant* are of great importance and should be chosen such that the noise is low (equals long time constant) and the sensitivity is high, without reaching saturation in the lock-in amplifier. Reducing the probe intensity will also make it possible to increase the sensitivity.

## A.6 Measurements

The lock-in amplifier is now ready for measurements.

# Appendix B

# Auto-Correlator

## B.1 Auto-correlator

This appendix outlines the procedure on how to use an auto-correlator. The first thing to make sure of is that the laser beam does not exceed the damage threshold.

## B.2 How to obtain a signal

**Back-reflection:** To be able to detect the signal, make sure that the height of the auto-correlator matches the height of the laser beam. Have the slid on so that it blocks the window in the front with the crossbar, and align the laser beam through the detection hole. Open the slid so that the window is visible again. If a reflection of the beam, a red dot, is not visible in the window; adjustments need to be made. Lock the front "legs" and pivot the the back leg to either side, you may also have to adjust the height up and down. With the combination of height adjustments and pivoting, you should be able to see the laser in the window in front of the auto-correlator. Do adjustments until it's in the cross-section of the crossbar, and back-reflection is now complete. You should be able to see a signal of the pulse on the display of the auto-correlator.

**Beam distance:** To get the correct and best signal further calibrations needs to be optimized. A knob on the right hand side of the auto-correlator is used for adjusting the beam distance. Adjust this back and forth while watching the display and see how the signal varies. By trial and error, set the beam distance to the maximum value displayed on the screen.

**Focus:** The last parameter that needs to be optimized is the focus. The knob for this is on the left hand side of the auto-correlator, and proceed the same way as for the beam distance. When the maximum value of the signal is found, the auto-correlator is now all set for use.

## B.3 Measurements

**Parameters:** To get good measurements, certain parameters may have to be adjusted which can be found on the screen. Set these values to proper values for your signal. For the laser

beam used in this experiment, set the parameters to:
- Scan = 1,5ps
- Average = off
- Smooth = off
- Sensitivity = 3
- Gain = 1 (But this can be adjusted without altering your result too much except increase the displayed signal on the screen)
$\alpha = 17$

**Cursors:** The auto-correlator calculates and give you the FWHM directly on to the screen, but for this to be correct the cursors need to be set properly. The horizontal cursors needs to be adjusted to the maximum height of the signal and the bottom, the auto-correlator have a built in cursor for the mean value. Adjust the vertical cursors to the points where the mean value cursor and the pulse meet. The correct FWHM should now be displayed on the screen and you will get the $\Delta t$ for the pulse.

# Appendix C

# Matlab code

## C.1 Plotfreq

Plotfreq.m normalize the temporal signal and calculates its frequency spectrum.

```
%%%%%%%%%%%%%%%%%%%%%%%%%%%%%%%%%%%%%%%%%%%%%%%%
%
%  MISC. PARAMETERS
%
%%%%%%%%%%%%%%%%%%%%%%%%%%%%%%%%%%%%%%%%%%%%%%%%
warning off MATLAB:divideByZero
clc; clear all; close all; clf;
format long;

%%%%%%%%%%%%%%%%%%%%%%%%%%%%%%%%%%%%%%%%%%%%%%%%
%
%  DATA PREPARATION
%
%%%%%%%%%%%%%%%%%%%%%%%%%%%%%%%%%%%%%%%%%%%%%%%%
load('smcstep_2012-04-25T1051.mat')     % Load data file
data = retval;

amp = data(:,1);
amp = flipud(amp);
ave = sum(amp)/length(amp)
nvec = length(amp)
ave_vec = ave*ones(nvec,1);
amp_norm = amp - ave_vec;

tmax = (nvec-1)*67e-15;                 %Temporal resolution

%%%%%%%%%%%%%%%%%%%%%%%%%%%%%%%%%%%%%%%%%%%%%%%%
%
%  FFT PARAMETERS
%
%%%%%%%%%%%%%%%%%%%%%%%%%%%%%%%%%%%%%%%%%%%%%%%%
n = 14;                                 % Radix-2 multiplier
N = 2^n;                                % Number of points
%N = nvec_ref;
t = 0:67e-15:tmax;                      % Time axis
Ts =  t(2)- t(1);                       % Time step
```

```
fs = 1/(N*Ts);                                  % Frequency step
freq =fs*(-N/2:(N-1)/2);                        % Frequency axis
%%%%%%%%%%%%%%%%%%%%%%%%%%%%%%%%%%%%%%%%%%%%%%

%%%%%%%%%%%%%%%%%%%%%%%%%%%%%%%%%%%%%%%%%%%%%%
%
%  FFT
%
%%%%%%%%%%%%%%%%%%%%%%%%%%%%%%%%%%%%%%%%%%%%%%
amp_freq = fftshift(fft(amp_norm,N))*N;

%%%%%%%%%%%%%%%%%%%%%%%%%%%%%%%%%%%%%%%%%%%%%%
%
%  FIGURES
%
%%%%%%%%%%%%%%%%%%%%%%%%%%%%%%%%%%%%%%%%%%%%%%
figure(1)
plot(t*10.^12,amp_norm);set(gca,'FontSize',16)
axis([0 inf -inf inf])
title('Time-domain','FontSize',18, 'FontWeight', 'bold');
xlabel('Time [ps]', 'FontSize', 16);
ylabel('V(t)  [V]', 'FontSize', 16);

figure(2)
plot(freq*10.^-12,abs(amp_freq));set(gca,'FontSize',16)
axis([0 3 0 inf])
title('Frequency spectrum', 'FontSize', 18, 'FontWeight', 'bold');
xlabel('Frequency [THz]','Fontsize',16);
ylabel('V(\omega)', 'FontSize', 16);
```

## C.2 Plothans

Plothans.m calculates the electric field strength, $E_{THz}$, of the measured signal. To use this script; double-click on the data file to temporary store the file as retval. Enter the number for the wanted type of case (usually 1) and the number for the step length of the translation stage (0.01 for most of the measurements performed in this thesis). A typical command will look like; plothans(retval, 1, 0.01).

```
function retval=plothans(scanVal,RT,stepLength)

%PLOTSMCSTEP plots the X and Y or R and theta values of a smcstep array
%
%scanVal is an array of smcstep values,
%i.e. four columns of X,Y,R,theta values
%RT can be one of four values:
%   0: X Y Raw
%   1: R T Raw
%   2: X Y Dev
%   3: R T Dev

retval=2;
ERROR=1;
SUCCESS=0;

```

```
scanValflip = flipud(scanVal);
stepTime = 2*stepLength*10/3;
scanDev = scanVal - repmat(mean(scanVal),length(scanVal),1);
temp = scanValflip(:,3);
sum = 0;

refsteps = 50;

for j=1:refsteps,
    sum = sum + temp(j);
end

average = sum/refsteps;

for j=1:length(scanVal),
    temp_zero(j) = ((temp(j) - average)/average);
end

switch RT
case 0
    A = 'X';
    B = 'Y';
    rawdev = 'raw';
    plotVal = scanVal;
case 1
    A = 'R';
    B = 'theta';
    rawdev = 'raw';
    plotVal = scanValflip;
case 2
    A = 'X';
    B = 'Y';
    rawdev = 'dev';
    plotVal = scanVal - repmat(mean(scanVal),length(scanVal),1);
case 3
    A = 'R';
    B = 'theta';
    rawdev = 'dev';
    plotVal = scanVal - repmat(mean(scanVal),length(scanVal),1);
otherwise
    disp('Unknown choice')
    retval=ERROR;
    return
end

x = (1:length(plotVal))*stepTime;
y = plotVal(1:end,1 + 2*mod(RT,2));

figure(1)
figure('Name',[A ' ' rawdev ' value']);
plot (x,y,'b-');set(gca,'FontSize',16)
grid on;
title('Time-domain', 'FontSize', 18, 'FontWeight', 'bold')
xlabel('Time delay in picosecond [ps]', 'FontSize', 16)
ylabel('V(t) [V]', 'FontSize', 16)
axis([0 inf -inf inf]);

x2 = (1:length(plotVal))*stepTime;
y2 = temp_zero*1.89*10^4;

```

```
figure(2)
figure('Name',[A ' ' rawdev ' value']);
plot(x2,y2,'b-');set(gca,'FontSize',16)
axis([0 inf -14e3 14e3]);
grid on;
title('Time-domain', 'FontSize', 18, 'FontWeight', 'bold')
xlabel('Time delay in picosecond  [ps]', 'FontSize', 16)
ylabel('E_T_H_z  [V/cm]', 'FontSize', 16)


retval=SUCCESS;
return;
```

## C.3 THz-TDS analysis

The matlab script THz TDS analysis abs disp.m (with underlines) is used for the THz-TDS analysis to obtain the frequency spectrum, the absorption coefficient and the refractive index of the signal.

```
%%%%%%%%%%%%%%%%%%%%%%%%%%%%%%%%%%%%%%%%%%%%%%%
%
%  MISC. PARAMETERS
%
%%%%%%%%%%%%%%%%%%%%%%%%%%%%%%%%%%%%%%%%%%%%%%%
warning off MATLAB:divideByZero
clc; clear all; close all; clf;
format long;

%%%%%%%%%%%%%%%%%%%%%%%%%%%%%%%%%%%%%%%%%%%%%%%
%
%  DATA PREPARATION
%
%%%%%%%%%%%%%%%%%%%%%%%%%%%%%%%%%%%%%%%%%%%%%%%
load('smcstep_2012-05-18T1812.mat')     % Load Reference data
d_ref = retval;

load('smcstep_2012-05-18T1756.mat')     % Load Sample data
d_sam = retval;

amp_ref = flipud(d_ref(:,1));
ave_ref = sum(amp_ref)/length(amp_ref);
nvec_ref = length(amp_ref);
ave_vec_ref = ave_ref*ones(nvec_ref,1);
amp_norm_ref = (amp_ref - ave_vec_ref);

amp_sam = flipud(d_sam(:,1));
ave_sam = sum(amp_sam)/length(amp_sam);
nvec_sam = length(amp_sam);
ave_vec_sam = ave_sam*ones(nvec_sam,1);
amp_norm_sam = (amp_sam - ave_vec_sam);

tmax = (nvec_ref-1)*67e-15;

%%%%%%%%%%%%%%%%%%%%%%%%%%%%%%%%%%%%%%%%%%%%%%%
```

```
%
% THICKNESS L OF SAMPLE
%
%%%%%%%%%%%%%%%%%%%%%%%%%%%%%%%%%%%%%%%%%%%%%%%

%Ref sample
Labs1 = 0.000;          %cm
Ldisp1 = 0.00000;       %m

%Sample
Labs2 = 0.0530;          %cm
Ldisp2 = 0.000530;       %m

Labs = Labs2 - Labs1;
Ldisp = Ldisp2 - Ldisp1;

%%%%%%%%%%%%%%%%%%%%%%%%%%%%%%%%%%%%%%%%%%%%%%%
%
%  FFT PARAMETERS
%
%%%%%%%%%%%%%%%%%%%%%%%%%%%%%%%%%%%%%%%%%%%%%%%
n = 14;                                  % Radix-2 multiplier
N = 2^n;                                 % Number of points
t = 0:67e-15:tmax;                       % Time axis
Ts =  t(2)- t(1);                        % Time step
fs = 1/(N*Ts);                           % Frequency step
freq =fs*(-N/2:(N-1)/2);                 % Frequency axis
%%%%%%%%%%%%%%%%%%%%%%%%%%%%%%%%%%%%%%%%%%%%%%%

%%%%%%%%%%%%%%%%%%%%%%%%%%%%%%%%%%%%%%%%%%%%%%%
%
%  FFT
%
%%%%%%%%%%%%%%%%%%%%%%%%%%%%%%%%%%%%%%%%%%%%%%%
amp_freq_ref = fftshift(fft(amp_norm_ref,N))*N;
amp_freq_sam = fftshift(fft(amp_norm_sam,N))*N;

%%%%%%%%%%%%%%%%%%%%%%%%%%%%%%%%%%%%%%%%%%%%%%%
%
%  ADDITIONAL PARAMETERS
%
%%%%%%%%%%%%%%%%%%%%%%%%%%%%%%%%%%%%%%%%%%%%%%%

c = 3*10.^8;
omega = 2*pi*freq;

%%%%%%%%%%%%%%%%%%%%%%%%%%%%%%%%%%%%%%%%%%%%%%%
%
%  TDS
%
%%%%%%%%%%%%%%%%%%%%%%%%%%%%%%%%%%%%%%%%%%%%%%%
E0p = real(amp_freq_ref);
E0dp = imag(amp_freq_ref);

Ep = real(amp_freq_sam);
Edp = imag(amp_freq_sam);
E_num = (E0p.*Edp-E0dp.*Ep);
E_den = (E0p.*Ep+E0dp.*Edp);
absfreq = (log((E0p.^2+E0dp.^2)./(Ep.^2+Edp.^2)))/Labs;
dispfreq = (c*(-unwrap(atan2(E_num,E_den)))).*(omega'*Ldisp);
```

```
96
97  %%%%%%%%%%%%%%%%%%%%%%%%%%%%%%%%%%%%%%%%%%%%
98  %
99  %  FIGURES
100 %
101 %%%%%%%%%%%%%%%%%%%%%%%%%%%%%%%%%%%%%%%%%%%%
102 x11 = t*10.^12;
103 y11 = amp_norm_ref;
104 x12 = t*10.^12;
105 y12 = amp_norm_sam;
106
107 figure(1)
108 plot(x11,y11,x12,y12,'r');set(gca,'FontSize',16)
109 axis([0 inf -inf inf])
110 legend('Ref','Si_3N_4', 'FontSize', 16, 'Location', 'SouthEast');
111 title('Time-domain','FontSize',18, 'FontWeight', 'bold');
112 xlabel('Time [ps]', 'FontSize', 16);
113 ylabel('V(t)  [V]', 'FontSize', 16);
114
115 x21 = freq*10.^-12;
116 y21 = abs(amp_freq_ref);
117 x22 = freq*10.^-12;
118 y22 = abs(amp_freq_sam);
119
120 figure(2)
121 plot(x21,y21,x22,y22,'r');set(gca,'FontSize',16)
122 axis([0.4 3 0 inf])
123 legend('N_2 - Ref','N_2 - Si_3N_4', 'FontSize', 16)
124 title('Frequency spectrum', 'FontSize', 18, 'FontWeight', 'bold');
125 xlabel('Frequency [THz]','Fontsize',16);
126 ylabel('V(\omega)', 'FontSize', 16);
127
128 figure(3)
129 plot(freq*10.^-12,absfreq);set(gca,'FontSize',16)
130 axis([0.4 2.5 0 40])
131 legend('N_2 - Si_3N_4', 'FontSize', 16)
132 title('Absorption coefficient', 'FontSize', 18, 'FontWeight', 'bold');
133 xlabel('Frequency [THz]', 'FontSize', 16);
134 ylabel('\alpha [cm^-1]', 'FontSize', 16);
135 grid on;
136
137 figure(4)
138 plot(freq*10.^-12,dispfreq);set(gca,'FontSize',16)
139 axis([0.4 2.5 0 10])
140 legend('N_2 - Si_3N_4', 'FontSize', 16)
141 title('Refractive index', 'FontSize', 18, 'FontWeight', 'bold');
142 xlabel('Frequency [THz]', 'FontSize', 16);
143 ylabel('n', 'FontSize', 16);
144 grid on;
```